An Advanced Classification System for Processing Multitemporal Landsat Imagery and Producing Kyoto Protocol Products

By

Hao Chen
B.Sc., Beijing University of Iron and Steel Technology, China, 1983

A Thesis Submitted in Partial Fulfillment of the
Requirements for the Degree of

MASTER of SCIENCE

In the Department of Computer Science

Supervisor: Dr. David G. Goodenough

Abstract

Canada has 418 million hectares of forests, representing 10% of the forested land in the world [1]. In 1997, Canada signed the Kyoto Protocol and agreed to cut greenhouse gas emissions by six percent below the 1990 level between 2008 and 2012 [2]. This agreement was ratified in December 2002. It requires Canada to report Canada's sustainable forest resources, including information about forest carbon, afforestation, reforestation, and deforestation (ARD). To fulfill this commitment, effective and accurate measuring tools are needed. One of these tools is satellite remote sensing, a cost-effective way to examine large forested areas in Canada for timely forest information. Historically, the study of forest aboveground carbon was carried out with detailed forest inventory and field sampling from temporary and permanent sample plots, which severely limited the forest area that could be studied. For regional and global scales, it is necessary to use remote sensing for aboveground carbon and ARD mapping due to time and financial constraints. Therefore, the purpose of this research is to develop, implement, and evaluate a computing system that uses multitemporal Landsat satellite images [3] to estimate the Kyoto-Protocol-related forest parameters and create geo-referenced maps, showing the spatial distribution of these parameters in a Geographic Information System (GIS). The new computing system consists of a segment-based and supervised classification engine with feature selection functionality and a Kyoto-Protocol-products estimation unit. The inclusion of the feature selection reduces the large dimensionality of the feature space of multitemporal remote Landsat data sets. Thus, more images could be added into the data sets for analysis. The implementation of the segment-based classifiers provides more

accurate forest cover classifications for estimating the Kyoto Protocol products than pixel-based classifiers. It is expected that this approach will be a new addition to the current existing methodologies for supporting Canada's reporting commitments on the sustainability of the forest resources in Canada. This approach can also be used by other countries to monitor Canada's compliance with international agreements.

Table of Contents

List of Tables

List of Figures

Acknowledgements

I would like to give special thanks to my thesis supervisor, Dr. David G. Goodenough, for his supervision, support, and encouragement during my graduate study in Computer Science at University of Victoria. I would like to thank Dr. Daniela Damian, Dr. Olaf Niemann, and Dr. Jay Pearlman for their valuable and helpful comments and corrections. I would like to thank Andrew Dyk for his consultation and technical support in processing Landsat images and thank Dr. Don Shields and Sarah McDonald for their efforts in editing this thesis.

1 Introduction

Canada is the second largest country in the world and has 10% of the world's forests. To monitor its sustainable forest resources and to honour it's future-reporting commitments set by the Kyoto Protocols, Canada needs effective and accurate measuring tools, which are based on the best available science.

1.1 Kyoto Protocol

The Kyoto Protocol [4] is an international agreement for reducing greenhouse gas emissions from industrialized countries and slowing the global warming process. In December of 1997, the participating nations in the Conference of Parties, held by the United Nations in Kyoto, Japan, achieved the agreement that required the developed countries to reduce their greenhouse gas emissions by an average of 5% below 1990 levels over the period between 2008 and 2012. The Kyoto Protocol will credit countries, where increased afforestation and reforestation activities result in carbon stock increases during the commitment period and, conversely, debit countries where deforestation activities lead to carbon stock decreases.

Canada sighed the Kyoto Protocol in 1998 and agreed to reduce its greenhouse gas emission in the period 2008 and 2012 to 6% lower than in 1990 levels. Under the Kyoto Protocol, Canada must report its carbon accounting changes during the commitment period on areas affected by afforestation, reforestation, deforestation (ARD) against the 1990 base.

1.2 Carbon Budget Model

The current forest carbon accounting tool used by the Canadian Forest Service (CFS) is the Carbon Budget Model (CBM-CFS2) [5], a computer-simulation model for estimating and assessing the status of carbon distributions in Canadian forests. The CBM-CFS2 system is built on a knowledge base developed from detailed forest inventories, temporary and permanent sample plots, and includes growth and yield and timber planning models. CBM-CFS2 simulates forest carbon cycles, which is used to estimate the carbon components in forests and to model past, present, or future carbon dynamics. The CBM-CFS2 system has been used in reporting the carbon status in Canadian forests. CBM-CFS2 has its limitations. The carbon analysis conducted by CBM-CFS2 does not use remote sensing inputs for its carbon simulation. It relies on forest inventory data, which are not a unified time series. These data do contain errors due to the constraints of the sample data collecting process. The accuracy of the inventory data, therefore, becomes a bottleneck of the carbon simulation of the CBM-CFS2 model. Moreover, the outputs and predictions of CBM-CFS2 need to be validated. There have not been cost-effective ways yet at the national level to provide quantitative information about carbon systematically, reliably, and accurately since it would acquire going to the field and making actual carbon measurements.

1.3 Remote Sensing Approach to Carbon Accounting

Multispectral and multitemporal remote sensing has been used to manage forest resources over large areas effectively [6-8]. Such applications include forest-cover

identification, classification, change detection, and forest biomass estimations. How can multispectral and multitemporal remote sensing be used for the forest carbon accounting and how can remote sensing analysis techniques be automated and used to derive Kyoto Protocol products for the Canadian forests?

In this research, details of the structure of a new computing system that uses multitemporal Landsat images to estimate the Kyoto-Protocol-related forest parameters are described. The research was divided into six stages. The first stage was to review current software for processing remote sensing data and study the requirements for the new computing system for the dynamic accounting of Canadian carbon stocks and related forest products. The second stage was the software design, implementation, and system testing. During this stage, remote sensing data calibration was also carried out. The calibration included geometric correction and radiometry correction.

In the third stage, multitemporal segmentation was performed on the calibrated Landsat images. In the fourth stage, a ground-truth knowledge base was identified and constructed through Geographical Information System (GIS) databases and forest inventory maps. To allow adding more Landsat images to the fused multitemporal data set, a feature selection technique was implemented. The feature selection process reduced data redundancy in the original data set and provided the optimal feature subset for the classification process.

The fifth stage was the segment-based classification. The classification module provided four supervised classifiers: Euclidean Distance, Divergence, Maximum Likelihood and Adaptive Classifier. The Adaptive classifier was the combination of the Maximum Likelihood classifier and Divergence classifier and was used to deal with the

small segment problem. The final stage was to compute forested areas and produce the Kyoto Protocol products: forest carbon, afforestation, reforestation, and deforestation.

1.4 The Research Goal and Objectives

The goal of this research is to use computing science and remote sensing technologies to implement software and build an advanced computing system for systematically, reliably, and accurately creating Kyoto Protocol products with remote sensing data for forest inventory, forest carbon, and change detection. The system is also complementary to the current existing methodologies, such as CBM-CFS2, for supporting Canada's reporting commitments on the sustainability of the forest resources in Canada.

The research is directed by the following objectives:

- implementing procedures for processing multitemporal remote sensing data;
- creating and testing the required computing modules;
- conducting multitemporal segmentation and classification;
- assessing classification accuracies;
- computing afforestation, reforestation and deforestation;
- measuring aboveground carbon in forested areas;
- and comparing remote sensing carbon with inventory-based carbon.

1.5 Computing Structure

The goal is to produce Kyoto Protocol products for forests. Therefore, the new computing system must compute remote sensing aboveground carbon and ARD products. Since the aboveground carbon is calculated in forested areas and the forest change products are obtained by using post classification comparisons, an essential computational component in the new system is a segment-based classification unit that offers user accurate and effective tools for multitemporal remote sensing image classifications. The classification procedure includes segmentation, training statistics and classification.

The increased spectral bands in the feature space provide new challenges to multitemporal remote sensing data analysis. To reduce the number of spectral bands in multitemporal remote sensing imagery to a manageable level, another component needed in the computing system is the feature selection. The implementation of the feature selection offers users an optimal feature subset without having to evaluate the criteria for all possible combinations of features.

The last component in the computing system is the aboveground carbon and ARD unit, which computes aboveground carbon and ARD distribution maps and statistics based on multitemporal classification images. The detailed computing system design is described in Chapter 4.

2 Landsat Satellite Imagery and Study Area

Landsat satellite images are used as the input data for the new remote sensing carbon computer system. The advantages of Landsat images over other remote sensing images such as Radar and Hyperspectral images are its long data reception period, mid-range spatial resolution, broad swath coverage, multispectral bands, availability, and affordability.

2.1 Landsat Satellite Data Reception Period

In 1972, the National Aeronautics and Space Administration (NASA) launched its first remote sensing satellite, Landsat-1. Since then the Landsat-series satellites, Landsat-2, 3, 4, 5 and 7, have been launched into space to explore, discover and monitor the earth's natural resources and provided uninterrupted earth surface images. Landsat-1, 2 and 3 finished their missions in 1978, 1982 and 1983, respectively. Landsat-4 and 5 are still in orbit, but in standby mode. Landsat-7 is the current operational satellite, providing data continuity with the early Landsat satellites and offering improved remote sensing technologies. The Landsat images have provided a unique resource for applications in agriculture, geology, forestry, regional planning, education, mapping, and global change research. NASA, now, is preparing to launch its next generation of the Landsat satellite, Landsat-8, in 2006. *Figure 1* shows the time line of data reception from Landsat satellite sequences [9].

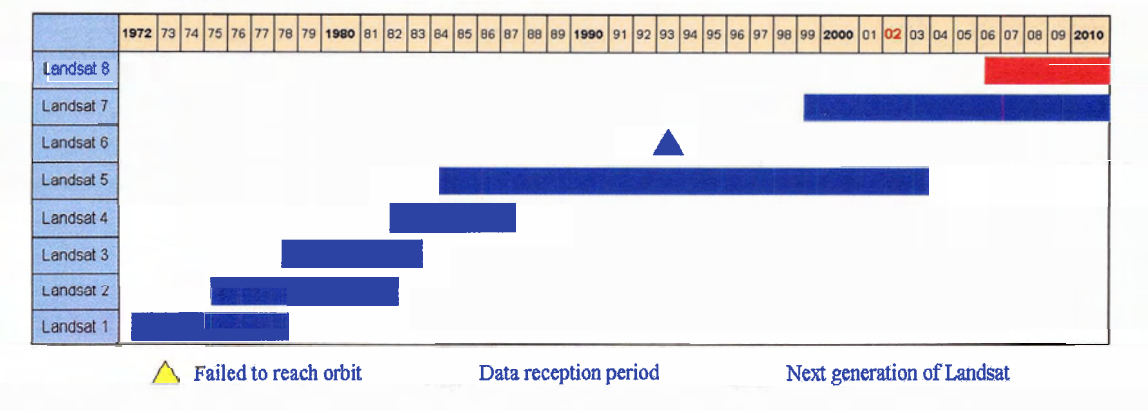

Figure 1. Time line of Landsat data coverage

This long data continuity of imaging the earth's surface from Landsat is a key factor for the new computing system to produce the Kyoto-Protocol-related products over the time frame between December 31, 1989 and December 31, 2012. Under the Kyoto Protocol, Canada is required to reduce its greenhouse gas emissions for all sectors by 6% below 1990 levels during the five-year commitment period from January 1, 2008 to December 31, 2012.

2.2 Landsat TM and ETM+ Sensor Characteristics

The Landsat images used for this study were acquired from Landsat-5 and Landsat-7, covering the period between 1985 and 2001. The imaging sensor mounted on Landsat-5 is the Thematic Mapper (TM), an advanced, multispectral scanning instrument designed to achieve high image resolution, spectral separation, geometric fidelity, and high radiometric accuracy [10]. The imaging sensor on Landsat-7 is called the Enhanced Thematic Mapper Plus (ETM+), an enhanced version of TM that provides data continuity with all of the previous Landsat sensors with the addition of a panchromatic band,

improved spatial resolution for the thermal band, and improved radiometric calibration equipment [11]. *Table 1* shows the detailed bandwidths of the TM sensor on the LANDSAT-5 and the ETM+ sensor on the Landsat-7 satellite [12].

Bandwidth (μ) of the TM and ETM+ Sensors								
Sensor	Band 1	Band 2	Band 3	Band 4	Band 5	Band 6 Thermal	Band 7	Band 8 Pan
TM	0.45 – 0.52	0.52 – 0.60	0.63 – 0.69	0.76 – 0.90	1.55 – 1.75	10.4 – 12.5	2.08 – 2.35	N/A
ETM+	0.45 – 0.52	0.53 – 0.61	0.63 – 0.69	0.78 – 0.90	1.55 – 1.75	10.4 – 12.5	2.09 – 2.35	0.52 – 0.90

Table 1. Comparison of spectral bands of TM and ETM+

The characteristics of the TM/ETM+ bands were selected to maximize their capabilities for detecting and monitoring different types of Earth resources [12]. Band-1 is designed for penetrating water and mapping along coastal areas. It is also useful for soil-vegetation differentiation and for distinguishing forest types. Band-2 is able to detect green reflectance from healthy vegetation. Band-3 can detect chlorophyll absorption in vegetation. Band 4 is ideal for determining vegetation types, vigour, and biomass content, for detecting water-land interfaces, and for soil moisture discrimination. Bands-5 and 7 are useful for vegetation and soil moisture studies and discriminating between rock and mineral types. Bands 1 to 5 and 7 have a spatial resolution of 30 metres and are quantized to 8-bits. Band-6 is a thermal-infrared band with a spatial resolution of 120 metres. Band-8 is a panchromatic channel of Landsat-7 providing a ground resolution of 15 metres. Both band 6 and band 8 are different from the other six multispectral bands in terms of their spatial resolutions and spectral characteristics. Therefore, they were not used in this study.

The swath width of the TM/ETM+ sensor is about 185 km. This broad swath in addition to the moderate spatial resolution of the six multispectral bands allows Landsat imagery to cover large areas on the Earth with enriched forest-vegetation information.

2.3 Study Area

The study area of this research is located near Hinton, Alberta [13]. It is about 285 km west of Edmonton and 85 km east of the town of Jasper. The size of the study area is approximately 2,700 km^2 with an elevation range from 1070 m above sea level in the east to 1725 m in its western extremity. There are four ecoregions in the area: Upper Boreal-Cordilleran (or Upper Foothills), Lower Boreal-Cordilleran (Lower Foothills), Subalpine and Montane, comprising 68%, 21%, 10% and 1% of the total area respectively. The forest stands in this region are dominated by lodgepole pine (*Pinus contorta Dougl. var. latifolia Engelm.*) and white spruce (*Picea glauca (Moench) Voss*). In the Lower Foothills, pure or mixed stands of trembling aspen (*Populus tremuloides Michx.*) and balsam poplar (*Populus balsamifera L.*) are interspersed with lodgepole pine and white spruce respectively. Black spruce (*Picea mariana (Mill.) B.S.P.*) and tamarack (*Larix laricina (Du Roi) K. Koch*) dominate in poorly drained areas.

Mature forest age of the dominant species varies between 80 and 110 years and stand heights are from 11 to 21+ metres [14]. The spatial distribution of stand heights is characterized by shorter stands in the northwest and broad patches of both taller and shorter stands to the southeast. Low to medium crown closure dominates most of the study area. The average stand volumes are generally less than 240 m^3/ha.

The area has been divided into Township-Ranges by the province. Each Township-Range is 100 km^2. A Landsat-5 TM image of the Hinton study area is illustrated in *Figure 2*. Cannel 5, 4, and 3 are shown as red, green, and blue channels. The white rectangles indicate the twenty-nine township-ranges (TWR).

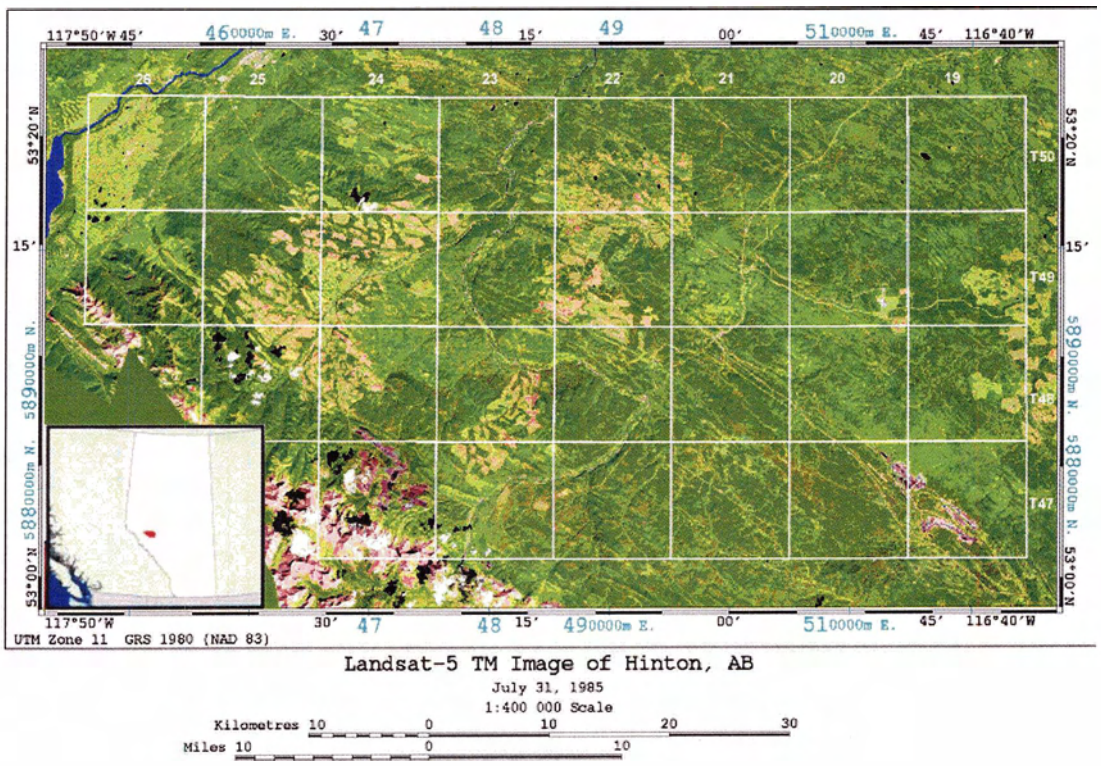

Figure 2. Landsat-5 TM image of the Hinton study site in Alberta, Canada

3 Current Software Packages and New System Requirements

Remote sensing data have been used to study the earth's surface for many years. There are many software packages that have been developed for processing remote sensing images. Yet, no off-the-shelf software products in place can systematically provide quantitative information for reporting remote sensing carbon and Kyoto Protocol products. One of the important functionalities a software package must provide for producing these products is the image classification, because all Kyoto-Protocol-related products are computed in classified woody areas.

3.1 Pixel-based vs. Segment-based Image classifiers

Pixel-based classification was originated in the 1970's and designed for classifying multispectral remote sensing data. The base unit is a pixel. During the classification, noise in remote sensing imagery may cause the spectral property of a pixel to be close to the spectral properties of other pixels representing different land-cover classes. As the result, high omission or commission errors may occur during the classification process. *Figure 3* (a) shows an example of the salt-and-pepper-like classification image over the northeast area of Hinton, Alberta, classified with a pixel-based Maximum Likelihood Classifier.

Unlike pixel-based classifiers, segment-based classification takes the digital number of neighbouring pixels into account. When these segments are classified, both the spectral and spatial properties are considered. Therefore, misclassification errors in the homogenous areas are reduced to the minimum. *Figure 3*(b) shows the segment-based

classification image from a segment-based Maximum Likelihood Classifier on the same area as that of *Figure 3* (a). *Figure 3* (b) is much clearer than *Figure 3* (a).

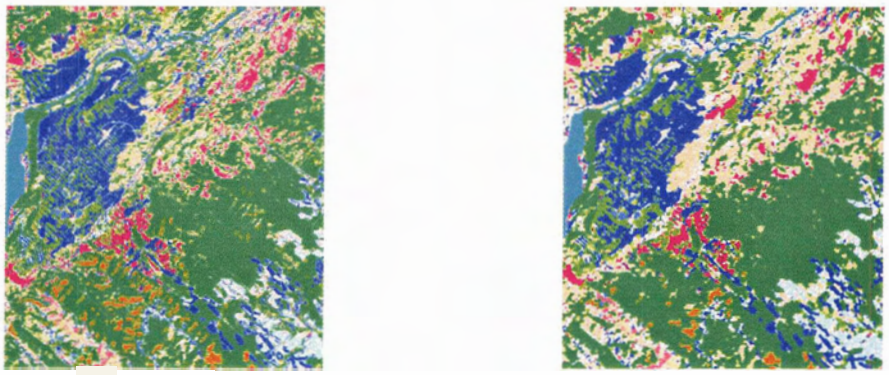

(a) Pixel-based (b) Segment-based

Figure 3. Comparison between pixel and segment-based classification images

Classification accuracies can be obtained from confusion matrixes, which provide information on how much of each original training area was actually classified into the intended class. If many pixels in the training areas are classified into different classes other than the intended ones, the classification accuracy will be low and the classification result will be not acceptable. The average accuracy in the confusion matrix is the average of the accuracies for each class. The overall accuracy in the confusion matrix is based on the weighted average of the individual classification accuracies assessed by the test areas. Thus, the more accurate estimates from larger training samples, the more heavy the weighting in the overall accuracy.

The comparison of the classification accuracies between the pixel-based and spatial-based classifications is shown in *Table 2*. The average classification accuracy of the spatial-based classification is about 9% higher than a pixel-based classifier for forest

classes. The overall classification accuracy of the spatial-based classification is more than 10% higher than the pixel-based classifier. Clearly, the spatial properties of the segments help to reduce noise in the remote sensing data.

	Spatial-based	Pixel-based
Classification Accuracy	Euclidean Distance	Minimum Distance
Average	81.4%	70.5%
Overall	94.2%	82.4%

Table 2. Comparison example between pixel-based and segment-based classifications in the Hinton study area

3.2 Commercial Classification Software

The most commonly used commercial software package for processing remote sensing imagery in Canada is the EASI/PACE Image Analysis System, provided by PCI Geomatics [15]. The software package has three built-in supervised classifiers for users to choose. These classifiers are: Parallelepiped, Euclidean Distance, and Maximum Likelihood Classifier, which are pixel-based classifiers.

ENVI [16] is another integrated image-processing program for remote sensing and is mainly used in the United States. The built-in classifiers in ENVI are Parallelepiped, Minimum Distance, Mahalanobis Distance, Maximum Likelihood, Spectral Angle Mapper, and Binary Encoding. Although ENVI has more built-in classifiers than PCI, they are all pixel-based classifiers.

eCognition [17] is a new spatial-based classification package. It uses the object-oriented programming design to segment remote sensing imagery and classify the segments with the nearest neighbour and fuzzy classifiers. This approach produces much

better classification accuracies than pixel-based classifiers. But, eCognition has its limitations. First, eCognition is a purely spatial-based classification program. It does not support any pixel-level image-processing operations and does not provide Application Programming Interface (API) for users to customize the system for their needs. Secondly, eCognition provides only two classifiers: Nearest Neighbour or Fuzzy Membership Functions. Thirdly, eCognition does not offer users feature selection functionality that plays an important role when processing multitemporal remote sensing images. Finally, eCognition works only on PCs under MS Windows operating system.

3.3 Other Classification Programs

PCI, ENVI, and eCognition are commercial software for remote sensing image classification. There are also other newly developed classification methods, which are used to overcome the limitation of the existing conventional classification methods and to improve the classification accuracy. One of the new methods is the Adaptive Bayesian Contextual Classification Based on Markov Random Fields (MRF) [18]. MRF is a spatial-based classifier, which creates homogenous segments with Markov Random Fields [19]. It also applies the Adaptive Classification Procedure to handle training classes that have fewer pixels in them [20].

Another new spatial-based classifier is Cluster-Space Classification scheme [21], which classifies remote sensing images by combining the supervised and unsupervised approaches. The unsupervised classifier generates a large number of homogenous clusters, and then the Maximum Likelihood Classifier is used for the image classification.

The above classification methods do take the account of the spectral and spatial properties of the remote sensing data. But, the segmentation procedures in these methods, such as MRF and Cluster-Space, are mainly focused on processing a single hyperspectral image. Moreover, these new methods have not been incorporated into any commercial software packages, such as PCI or ENVI.

3.4 Requirements for the New System

To provide quantitative information for remote sensing carbon and Kyoto Protocol products systematically and accurately, a new computing system is required. It should provide users advanced spatial-based classifiers, have the ability to classify multitemporal Landsat imagery with large dimensionality in the feature space, support forest carbon and ARD calculation, and can be used as a plug-in module for one of the commercial remote sensing software packages, such as PCI Geomatics.

Forest carbon measurements provided by the new computing system should be comparable with the results from CBM-CFS2, which uses growth curves to describe the dynamics of species groups: softwood, hardwood, and mixed wood in each ecosystem type [22]. These three forest types should be included in remote sensing classification.

4 Computing System Design

The new computing system was designed and implemented to derive Kyoto-Protocol products systematically and effectively from multispectral and multitemporal remote sensing images and is called the Kyoto Protocol Automated Classification System (KPACS). The KPACS outputs are geo-referenced GIS layers showing the spatial distribution of the forest parameters: forest cover, aboveground carbon, afforestation, reforestation, and deforestation (ARD). KPACS consists of six software modules: the segmentation module, training statistics module, feature selection module, classification module, carbon module, and ARD module.

4.1 Programming Flow Chart

Figure 4 is the block chart of the design of KPACS. The first unit is the image segmentation unit. It segments adjacent pixels in multitemporal Landsat imagery with respect to their spectral characteristics to form relatively homogenous areas. By adjusting the homogeneity-level threshold parameter in the program, the smoothness of segments is controlled. The second unit is the training knowledge acquisition unit. It calculates the statistics of training data collected from fieldwork, GIS databases, or paper maps and trains the computing system to have the ability to recognize features that are similar to the training data. The third unit is the feature selection unit. It uses the knowledge gained from the training process to select an optimal feature subset from the original feature group for the image classification process. The feature selection allows more collections of Landsat data at different dates to be added to the multitemporal classification and

carbon analysis. The fourth unit is the classification unit. It classifies the segments in the multitemporal Landsat imagery with its training knowledge base. Users are able to choose different classifiers for the supervised classification. A forest cover map is generated in this step. The last unit is the Kyoto Protocol products unit. It computes carbon, afforestation, reforestation, and deforestation in the forested areas and produces images showing spatial distributions of these products.

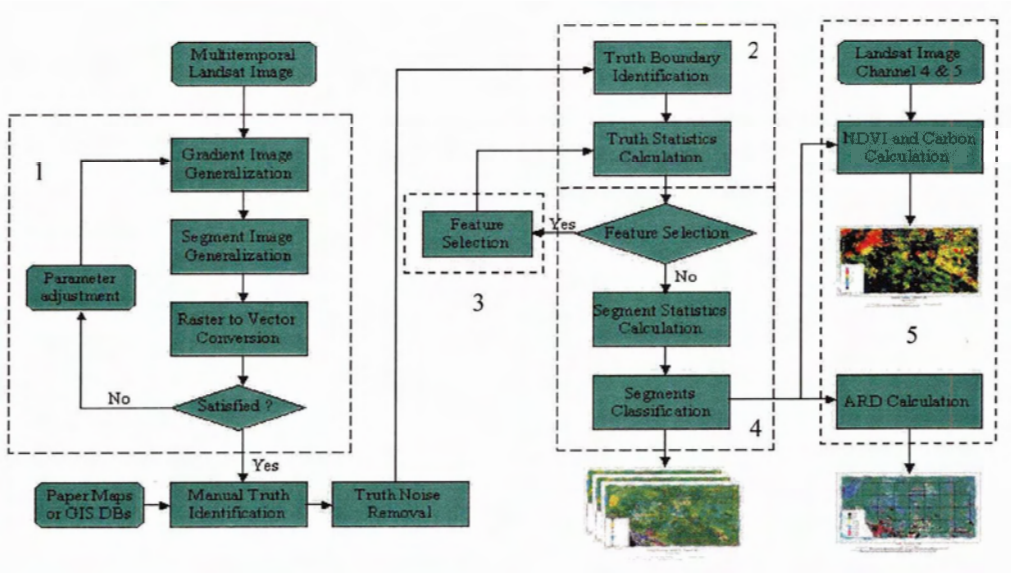

Figure 4. KPACS computing system block chart

4.2 Image Segmentation

Segmentation is a process of grouping adjacent pixels in a remote sensing image, based on their intensity values in one or more features, and partitioning the image into homogeneous segments. The method used for creating segments is the valley-seeking algorithm [23, 24].

The algorithm calculates the intensity of each pixel in the image corresponding to the difference between each pixel in the original image and its neighbours. The maximum differences computed from one or more of the input channels are used to create a gradient image. The valley-seeking algorithm inverts the pixel values in the gradient image so that ridges of the great differences between pixels and their neighbours become the valleys. The program then follows the valleys to create segment boundaries.

The homogeneous level of smoothness of a segment is controlled by a threshold parameter. A ground object may not be homogeneous in every image band. This will cause the object to have more segments in the segmentation process. These segments, however, can be integrated to the same general class during the classification process.

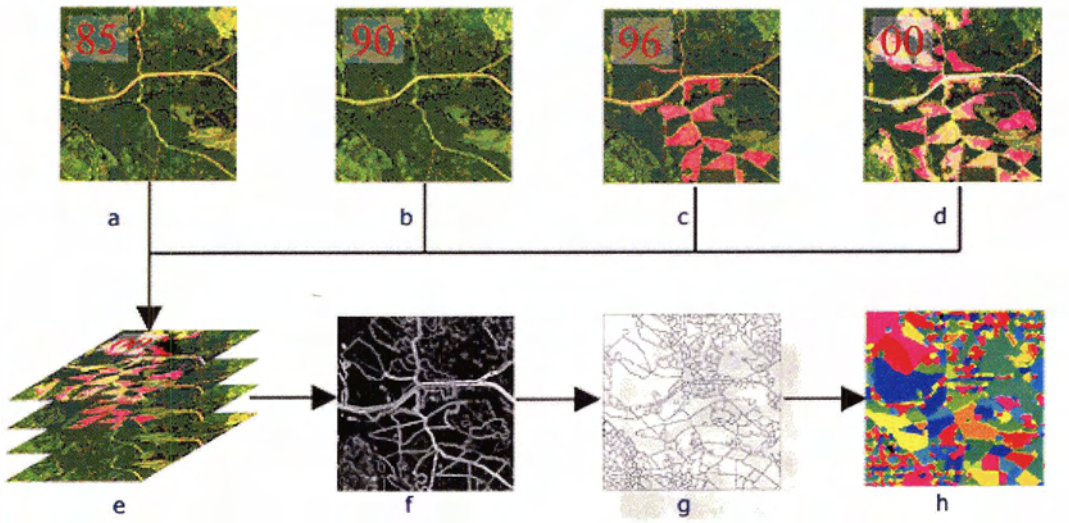

Figure 5. Segmentation process

Figure 5 shows an example of the segmentation process. Four Landsat images (*Figure 5a, 5b, 5c, 5d*) were collected from 1985, 1990, 1996, and 2000 respectively and

fused to create a multitemporal data set (*Figure 5e*), which contains 24 multispectral image channels. A gradient image (*Figure 5f*) was generated from the multitemporal data set. The bright edges in the gradient image illustrate the maximum difference of the intensities between image pixels. Next, the gradient image was converted to a valley image (*Figure 5g*) by reversing intensity values in the gradient image. The bright edges then become to dark valleys. Finally, the program followed the valleys and used the homogeneity control to generate a segmented image (*Figure 5h*). Each segment is assigned with a unique segment ID.

The method of calculating the intensity of a pixel in the gradient image is to sum the maximum value of the absolute differences for each neighbour in the feature space over a 3×3 window [25]. The process is initiated from the top-left corner of the image and moves down to the right. The elements in the window for Band k covering the top-left corner of the image are represented by (1).

$$3\times3 \text{ window for Band } k = \begin{bmatrix} X_{11k}, X_{12k}, X_{13k} \\ X_{21k}, X_{22k}, X_{23k} \\ X_{31k}, X_{32k}, X_{33k} \end{bmatrix} \qquad (1)$$

$$Y_{22} = \sum_{i=1}^{3} \sum_{j=1}^{3} \underset{k=1}{\overset{N}{\text{Max}}} | X_{ijk} - X_{22k}| \qquad (2)$$

The intensity of the centre pixel can be written as in (2), where X_{ijk} is the input-pixel value of line i and pixel j from Band k, N is the total number of input bands, and Y_{22} is the gradient value of the centre pixel in the 3x3 matrix in the gradient image.

In detail, three image lines from the input spectral bands are read into an image buffer, and the gradient value in the 3x3 window is calculated. After the computation of each line, the resulting gradient line is written into the gradient image. To calculate the border pixels in the image, the pixels that echo the image over the image border pixels are used for this special case. The results of the calculated gradient values are stored in the gradient image file.

The segmentation process involves three passes over an inversed gradient image, which inverses the intensity of pixels in the initial gradient image. The edge pixels (having the highest values in the region) in the gradient image become the valley pixels (having the lowest values in that region) in the inversed gradient image. Each segmentation pass processes three lines at a time.

The first pass is an initial segmentation process. For each pixel the program computes which of its neighbours has the lowest value in all eight directions. The results are stored in a temporary file. In the second pass, the program generates a preliminary segment image by following the link defined in the first pass and expanding pixels into homogeneous areas. The segments are all surrounded by the valley pixels.

The preliminary segmentation image needs to be optimized. Noise in a homogeneous region of the input multispectral image may split the homogeneous field into several segments. Therefore, the third pass of the segmentation process identifies these invalid segments and merges them into one valid homogenous area based on the selection of the smoothness value. If the smoothness parameter value is set to "0", no segment fusion occurs. Otherwise, the higher the value is, the smaller the number of

segments in the segmentation image. The third pass produces the final segmentation image as an output, and each of the segments has a unique identification number.

4.3 Training Knowledge Base for Supervised Classification

Remote sensing classification is the process of assigning image pixels or segments, based on their spectral and spatial properties in the image, into a finite number of individual classes or categories. If a pixel or a segment meets a set of criteria, this pixel or segment is assigned to that class corresponding to the criteria. There are two main classification methods: supervised classification and unsupervised classification [26].

4.3.1 Supervised Classification

In supervised classification [12, 27], spectral signatures from user-specified locations are developed to create a training knowledge base. This process is also called the training process, which will train a classification program to have the ability of recognizing these land-cover categories of interest during the supervised classification. The training areas, such as water, vegetation, grassland, forest, and clearcut, can be identified with help from field-data collections, GIS vector layers, or paper maps containing natural resource information. Once the training areas are developed, statistics are calculated to generate spectral parametric signatures from the specified areas. These signatures are then saved in the training knowledge base and used to classify all pixels in the image. Supervised classification provides human controls to users so that it is able to

produce accurate and meaningful classification results. However, collecting training data sometimes may become very expensive or even impossible due to the level of accessibility of study areas. Thus, training data could contain errors due to inaccurate information sources or unclear class descriptions.

4.3.2 Unsupervised Classification

Unsupervised classification [12, 27] uses a statistical clustering approach to select separable spectral classes inherent in remote sensing data. Clustering is a more automated computing process, but the initial classification image is hard to interpret. Decisions need to be made concerning which land-cover classes correspond to which clusters. Prior knowledge about the study area is required to assign these clusters to the classes. It may take a user many trials to get meaningful results since the classes of interest may be mixed in several clusters.

4.3.3 Training Area Inhomogeniety

The supervised classification method was implemented for KPACS to provide accurate and meaningful classification results for measurements of the Kyoto Protocol products: aboveground carbon and ARD. The training knowledge base in KPACS was represented by a training image channel together with its corresponding statistics files. Training areas can be identified from field data, aerial photographs, GIS data, paper maps, and other information sources.

Before the training areas can be used for calculating spectral signature for each identified class, inhomogeniety caused by natural variation and edge effects in the training areas and by inaccurate information sources and unclear class descriptions should be separated or removed. A clustering technique for unsupervised classification, *K-Means* [28], can be used for this purpose. *K-Means* returns a clustering of data by minimizing the within-cluster sums-of-squares, given initial estimates for the cluster centres, so that the training data can be clustered to different regions within a training class. Each of the clusters will be evaluated. Erroneous training clusters will be ejected from the training areas, similar (small Bhattacharrya distances) small clusters will be merged or removed, and large clusters will be retained.

Different clusters that represent a training class can be aggregated into one original training class before the classification process or used as the subclasses of the original training class for the classification - the aggregation process is performed after the classification.

Figure 6 shows an example of using *K-Means* to eliminate inhomogeniety from a training area in the coniferous class. In *Figure 6* (a), a coniferous training area was selected. In *Figure 6* (b), the area was extracted to form a training mask. In *Figure 6* (c), *K-Means* was applied under the mask created in *Figure 6* (b). The training area was then broken into several clusters. The light green areas were the shaded parts in the coniferous forest area. The blue areas were the sunlit parts of the coniferous forest area. The pink areas showed the boundary effects. The yellow areas were actually the non-coniferous areas. To clean this training area, incorrect truth clusters such as yellow regions and pink

edges were removed. The remaining clusters representing the coniferous class were then the blue and green clusters in this example.

The blue and green clusters could be merged as one coniferous training area for the classification or used as two subclasses for the classification, depending upon how close the Bhattacharrya distance was.

(a) Coniferous Area (b) Training Mask (c) Clustering Results

Figure 6. Homogeneities in a coniferous training area

4.4 Training Statistics Generation

When a training image is created, KPACS computes the spectral statistics of the training areas from all spectral bands, which are then used to train the classifiers for recognizing spectrally similar areas for each class. The spectral statistics include mean, covariance, determinants and parallelepiped volumes.

4.4.1 Small Training Sample Problem

Due to a larger number of multispectral bands in a multitemporal remote sensing image, the training areas should have enough training pixels in each training class,

especially when supervised classifiers relying on training-class statistics, such as mean and covariance, are involved. The basic rule for making training areas is that for p-dimensional data, more than p+1 samples are required in each class [18]. Otherwise, the sample covariance matrix estimate is singular and unusable.

4.4.2 Parametric Statistics of Training Classes

The first step in obtaining the training statistics is to determine the training-field boundaries in the training image [29]. The second step is to compute the training statistics of the training classes from all multispectral image bands [30]. The outputs are stored into two internal files. One is called the "truth" file, containing all information about the training-segment boundaries. The other is called the "statistics" file, containing all statistics information for each training class.

To determine the training segment boundaries, the boundary identification module in KPACS checks the training image size first, and then it starts looping through the training image band and reading one line at the time into the image buffer. Each pixel value in the line is examined for a change of the class identification. When the current pixel is a start point of a class record, the program sets the flag to "reading" and remembers the class number and line number. When the current pixel is the end point of the training record or the end of the current line, the program inserts the class record into the truth file and sets the flag back to the initial state.

To calculate the Gaussian statistics for a training class, the program acquires the total number of training records of the class from the truth file and loops through each of them sequentially. It remembers the line number, start and stop pixel, and class number

of each training record. The corresponding pixels in the multispectral bands of the remote sensing image are then retrieved and saved to an image buffer. Next, the statistics such as mean, covariance, determinants, parallelepiped volumes and lower and upper intensity values of the class are computed. The statistical results of all training classes are stored in the training statistics file.

4.5 Feature Selection

Using remote sensing as an approach to report carbon, afforestation, reforestation, and deforestation under the Kyoto Protocol during the committed time frame requires KPACS having the ability to process multitemporal remote sensing data. Fused multitemporal imagery result in many more spectral bands in the feature space. The increased data volume causes increased image processing time. Moreover, a larger number of training pixels for each class are required in order to avoid inaccurate estimates of covariance matrices when statistics-based classifiers are used. In addition, computing hardware and software may also limit the number of spectral bands that can be used in the classification process. To overcome these challenges, a feature selection module is implemented and integrated into KPACS.

When working with multitemporal remote sensing imagery, some multispectral bands are highly correlated. Such bands may not contribute any additional information to the classification. Therefore, by using feature selection techniques, an optimum subset from the original feature group can be selected in order to reduce data redundancy with little reduction in classification accuracy. Moreover, the use of feature selection keeps the number of spectral bands at a level such that the training data do not have to be increased.

One of the common approaches to the feature selection implementation is the exhaustive evaluation of a criterion for all subsets of size m from a set of n spectral bands to select the best subset. A user specifies a desired m from an n-band imagery. The best feature set is the one that yields the maximum value of the criterion among all subsets of m features. For example, if m = 2 and n = 6 the algorithm compares criterion values among all of the (6/2)=(6!)/(2!(6-2)!)=15 subsets and selects a subset having the maximum criterion value. If m = 12 and n = 24 the algorithm needs to go through all of the 2,704,156 subsets to find the best subset. The exhaustive approach certainly can offer the best subset of m features from the n-band imagery, but becomes much more computationally expensive when n gets larger [31].

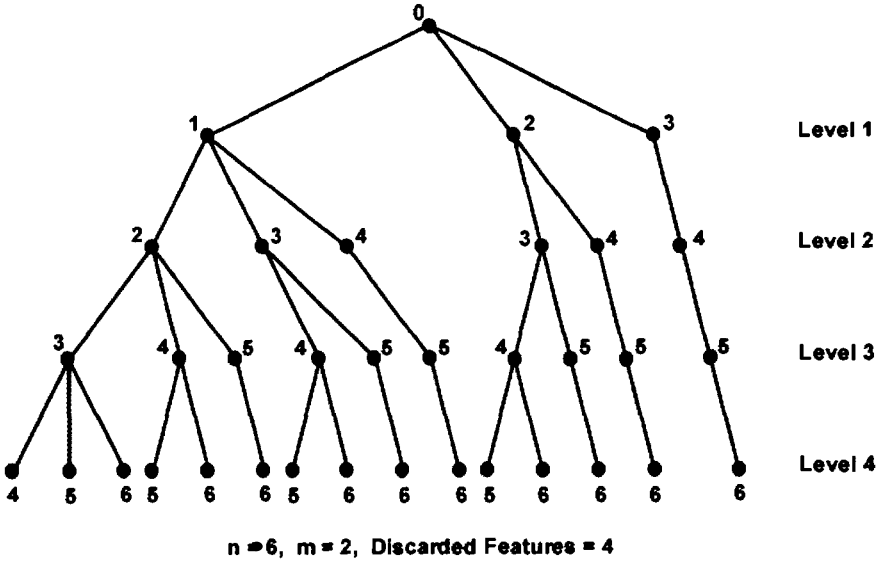

Figure 7. Branch and bound solution tree

Another approach is to apply sub-optimal selection schemes such as the branch-and-bound algorithm. The branch and bound algorithm [32] uses a solution tree to

compute an optimum subset from a feature group. *Figure 7* shows an example of the branch-and-bound solution tree, where n is 6 and m is 2. The number of the unwanted features is 4. Each node in the tree represents a spectral band that can be dropped out. For example, Node (1) is the dropped Band-1 in the data set.

In the initial stage, the algorithm sets a preliminary bound value B, which is the current best criterion value of an arbitrary subset Z of m, and an initial band list containing the n spectral features. Next, the algorithm starts with the complete set of n features to systematically evaluate bound values for the subsets of size greater than or equal to m. For example, it drops Band-1 in Level 1 and then evaluates the bound value for this subset. If the new bound value is less optimal than B it means that Band-1 cannot be dropped. The algorithm stops the expansion of examining all m-feature subsets in the Band-1 sub-tree since any feature subset without Band-1 will have a bound value less optimal than the previous B (assumption of the monotonicity of the criterion [32]). The algorithm then tracks back to the previous level (Level 0) and selects the next unexplored node (Band-2) to repeat the evaluation.

If the bound value after dropping Band-1 is better than B, it means that Band-1 can be dropped. The algorithm then moves to the next level (Level 2) and chooses the first unexplored node (Band-2) to see if this node (Band-2) can be dropped. The evaluation process continues. When it reaches the lowest level (Level 4) in the solution tree, the algorithm updates the bound value B and the optimal feature subset Z. The program then puts the leaf node back to the prior band list, tracks back to the previous level (Level 3), and starts evaluating the next available branch with the updated bound

value until it finishes the entire solution tree. At the conclusion of the algorithm the subset, Z, contains the optimal feature subset.

The advantage of the branch and bound algorithm is that the program is able to avoid exhaustive enumeration when systematically evaluating bound values in the solution tree. When a bound value at a node is less optimal than the previous bound value, the entire sub-tree of this node is eliminated from further expansion. Therefore, the algorithm is very efficient. However, the branch and bond algorithm only offers that the selected set of features is an optimal subset in the solution tree. It does not guarantee that the selected set is always the globally best one among all subset.

There are two reasons for that. One is the round-off error that happens in the criterion calculation process. When two criterion values are too close, the round-off error may cause the branch bound algorithm to make a wrong decision and reject a sub-tree that may contain the globally best subset. The second reason is due to noise in an input data set. The noise may vary criterion values. When two criteria get too close the globally best subset may be missed.

The criterion of the feature selection algorithm is the divergence. For Gaussian distributions, the calculation of divergence is based on the training class means and covariance matrices [31]. The divergence function is given by (3):

$$J_{ij} = \tfrac{1}{2} (M_i - M_j)^T (\Sigma_i^{-1} + \Sigma_j^{-1}) (M_i - M_j) + \tfrac{1}{2} \mathrm{Trace}(\Sigma_i^{-1}\Sigma_j + \Sigma_j^{-1}\Sigma_i - 2I) \qquad (3)$$

where J_{ij} is the separability measure between the two classes i and j, M_ℓ is the class sample mean, and Σ_ℓ is the class covariance matrix for class ℓ.

The function (3) has two parts: The quadratic term and the trace term. The quadratic term $(M_i - M_j)^T (\sum_i^{-1} + \sum_j^{-1}) (M_i - M_j)$ contains most of the discriminatory information in the divergence, especially when distance classifiers are used in the later classification process [31]. The computation of the quadratic term requires $O(n^2)$ operations, and the computation of the inverse of an *n* feature covariance matrix requires $O(n^3)$ operations. However, since the quadratic term can be implemented recursively when a feature is removed from and added to the feature subsets in the solution tree, the number of operations of computing the quadratic term can be reduced to O(n), and the number of computations for the inverse of an *n* feature covariance matrix can be reduced to $O(n^2)$ operations. This results in very considerable computational savings.

The computation of the trace term involves $O(n^2)$ operations in addition to $O(n^2)$ operations used in inverting an *n* feature covariance matrix. Therefore, the trace term dominates the computation time of evaluating divergence values. But, because the trace term contains less discriminatory information in the divergence, it can be implemented as a secondary option so that a user can decide if he/she wants to use the trace term for the divergence computation.

To measure the separability among multiple training classes, the average pairwise divergence, J_{APD}, can be used as the criterion (4):

$$J_{APD} = \sum_{i<j}\sum J_{ij} \; / \; [m\,(m-1)] \qquad (4)$$

J_{APD} is obtained by adding J_{ij} for all class pairs and then dividing the sum by the total number of the classes. The optimum feature subset should have the maximum divergence value.

To avoid domination by class pairs with large divergence values in the summation, two variants of the average pairwise divergence can be applied. One is called the Average Transformed Pairwise Divergence, J_{ATPD}, (5):

$$J_{ATPD} = \sum_{i<j}\sum \{2[1-\exp(-J_{ij} / 8)]\} / [m (m-1)] \qquad (5)$$

and the other is called the Minimum Pairwise Divergence, J_{MPD}, (6):

$$J_{MPD} = \min_{i<j} J_{ij} \qquad (6)$$

The simplified pseudo code of the branch and bound algorithm is given in Appendix A [33]. The above criteria are all based on mean values and covariance matrices of training classes. Thus, whenever there is a change in training data such as adding or deleting a training class to or from a multitemporal data set, the feature selection process needs to be repeated because different class sets may lead to different feature selection results.

4.6 Remote Sensing Image Classifiers

The KPACS system has four supervised spatial-based classifiers available. These classifiers are Euclidean Distance, Maximum Likelihood, Divergence, and Adaptive Classifier.

4.6.1 Euclidean Distance

Euclidean Distance is based on the concept of pattern classification by distance function [28]. The distances between training means and segment means are computed. A training class, which has the closest distance to a segment, is assigned as the class to this segment. The Euclidean distance between a segment and a training class is given by (5) [28]:

$$D_i = \| x - z_i \| = [(x - z_i)' (x - z_i)]^{1/2} \qquad (5)$$

where x is the mean value of an arbitrary segment, z is the mean value of a training class, and i is the ith Class. The Euclidean Distance classifier computes the distance D_i from a segment x of unknown classification to each of the training classes z_i and assigns the segment x to the class z having the lowest value of D.

The Euclidean Distance classifier is simple and quick because it uses only the means for each class being considered. But, the classification accuracy attained with this classifier is less accurate than the other three classifiers, which are discussed in the following sections.

4.6.2 Maximum Likelihood

The Maximum Likelihood classifier is a parametric classifier [34]. If Gaussian distribution is assumed, the classifier takes into account the statistical properties of remote sensing image data, i.e. means and covariances of the training classes. With these statistical properties, the likelihood of a segment belonging to a class is computed by

using the parameters given by the training data. The class having the maximum likelihood estimate will be assigned to the segment as the most likely class.

The likelihood $L\omega_i$ is defined as the posterior probability of a pixel belonging to Class ω_i, shown in (6) [34]:

$$L\omega_i = P(\omega_i /X) = P(\omega_i) \times P(X/ \omega_i) \ / P(X) \qquad (6)$$

where $P(\omega_i)$ is the prior probability of Class ω_i, X is the image data of *n* bands, $P(X/ \omega_i)$ is the conditional probability to observe X from class ω_i, and P(X) is the prior probability of X. If equal prior probabilities are assumed for all classes, $L\omega_i$ depends on $P(X/\omega_i)$ or the probability density function. For Gaussian data, a multivariate normal distribution is applied as the probability density function. When the Gaussian distribution is assumed in the ground training data of Class ω_i, the likelihood function can be written as (7) [34]:

$$L\omega_i(X) = (2\pi)^{-n/2} |C\omega_i|^{-1/2} EXP\{-1/2 \ (X - M\omega_i)^T \ C\omega_i^{-1} \ (X - M\omega_i)\} \qquad (7)$$

where X is the image data of *n* bands, $L\omega_i(X)$ is the likelihood of X belonging to Class ω_i, $M\omega_i$ is the mean vector of the ground truth data in Class ω_i, $C\omega_i$ is the covariance matrix of Class ω_i generated from the ground training data, and $|C\omega_i|$ is the determinant of $C\omega_i$.

The Maximum Likelihood classifier is an analytic maximization procedure and has an advantage from the point of view of the probability theory. But, the classifier is based on the assumption that the data population is the Gaussian distribution. When the population is not Gaussian, such as a Radar image with Poisson distribution, the Maximum Likelihood classifier cannot be applied. Furthermore, the Maximum Likelihood classifier relies on ground training data to estimate the mean vector and the

covariance matrix of population in (7). The number of elements in a covariance matrix varies as P(P-1)/2, where P is the dimensionality of the feature space. Therefore, sufficient training samples are required to ensure the estimation is valid [35].

4.6.3 Divergence

The Divergence classifier uses Function (3) to measure the separability between classes in a remote sensing image. The algorithm tries to find the smallest multi-dimensional distance between a segment's statistics and class statistics to assign the segment to a class. The classifier considers the statistical properties not only from the training classes, but also from the segment objects in the remote sensing image. But, like the Maximum Likelihood classifier, it requires sufficient training samples and cannot be applied to non-Gaussian data. It is also not recommended to apply it to a multitemporal remote sensing image with many small segments. (The high dimensionality in the feature space of multitemporal imagery results in many small homogeneous segments.) If a segment does not have enough pixels compared to the number of input multispectral bands, the classifier may produce poor classification results due to the ill-conditioned covariance matrix of the segment.

4.6.4 Adaptive Classifier

The Adaptive Classifier is designed to diminish the small-segment problem when using the Divergence Classifier on a multitemporal data set with high dimensionality. The Adaptive Classifier applies either the Maximum Likelihood classifier or the

Divergence classifier depending on the segment size. If the size of a segment is smaller than a threshold value, the Maximum Likelihood classifier is applied; otherwise, the Divergence classifier is used. The adaptive classifier improves the classification accuracy.

The threshold value for switching between the Divergence classifier and the Maximum Likelihood classifier relies on the number of spectral bands in the feature space. Since the number of elements in a covariance matrix of a segment increases as the square of the number of input bands, the threshold value is decided as (8):

$$\text{Threshold} = NF^2 + 1 \qquad (8)$$

where NF is the number of input multispectral bands. Because the Adaptive Classifier is a combination of the Maximum Likelihood classifier and the Divergence classifier, it requires enough ground training samples and cannot be applied to non-Gaussian data.

4.6.5 Classifier Comparison

Comparisons of the four classifiers were conducted on a 2001 Landsat image of the Hinton area with six multispectral bands. There were 12 classes involved in the classification and each training class had sufficient training pixels to estimate the mean vectors and the covariance matrices. *Figure 8* shows the class classification comparisons between the four different classifiers. In the image, EUD, DIV, MLC, and ADP stand for the Euclidean Distance classifier, the Maximum Likelihood classifier, the Divergence classifier, and the Adaptive Classifier respectively.

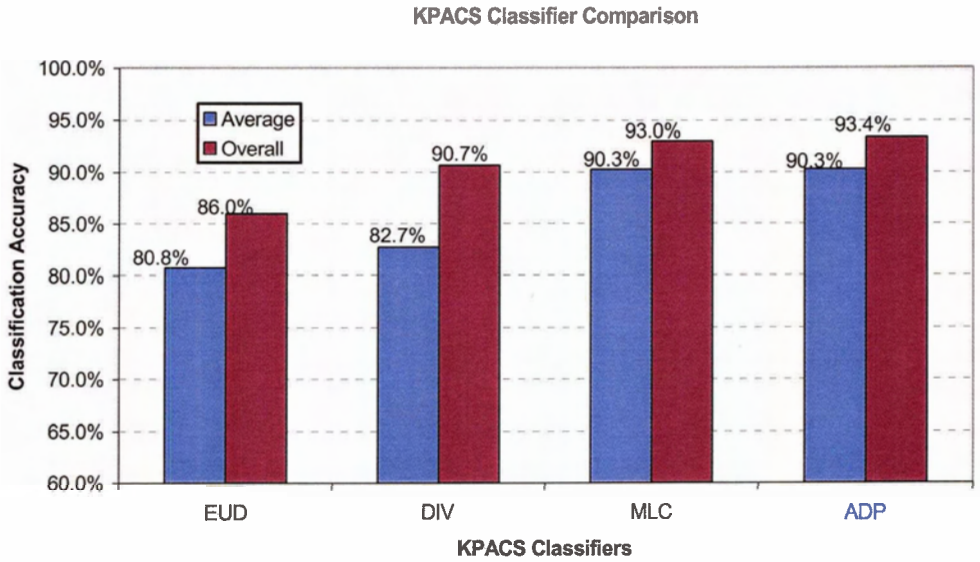

Figure 8. 2001 Landsat Classification with different classifiers

The Euclidean Distance classifier had the lowest classification accuracies in the comparisons. The Divergence classifier did better. The Maximum Likelihood classifier produced the second best of the classification accuracies, while the Adaptive Classifier had the best classification results in both the average and overall accuracies.

4.7 Aboveground Carbon Calculation

Remote sensing vegetation biomass and aboveground carbon are computed in forested areas, classified as Softwood, Hardwood, and Mixed wood in multitemporal Landsat classification imagery. The method for estimating forest biomass and carbon with Landsat data was published in [36, 37].

It is preferred that permanent sample plot data from the study area are used to develop the biomass relationship. This relationship is a function of remote sensing vegetation indices, forest class, site index, and age class. However, the permanent sample plot data of the Hinton study area were not available from the local forest management, Weldwood's Hinton Division [38]. Instead, the biomass relationship function (9) derived from the Canal Flats study site in southeast BC, which is similar in forest species to the Hinton study area, was used for this study [37].

$$\text{Biomass Volume } (m^3/ha) = -478.58 + 4.5041 \times \text{ND45} \qquad (9)$$

where ND45 is the vegetation index, averaged over an 11×11 pixel window. ND45 is defined as (10):

$$\text{ND45} = 128 \times [(\text{TM4} - \text{TM5}) / (\text{TM4} + \text{TM5})] + 128 \qquad (10)$$

where TM4 and TM5 are LANDSAT spectral channels calibrated for Band-4 and 5. The carbon function can then be written in (11):

$$\text{Carbon (kg/ha)} = \text{Biomass Volume} \times \text{Density} \times 0.5 \qquad (11)$$

Biomass Volume unit is m^3/ha. The Density is 409 kg/m^3, and the carbon unit is kg/ha. The density value is an average for the species in the study area [39]. The pixel size needs to be converted to hectares for computing the biomass and carbon for each pixel.

The computing procedure for calculating Landsat aboveground carbon in forested areas [40] is shown in *Figure 9*.

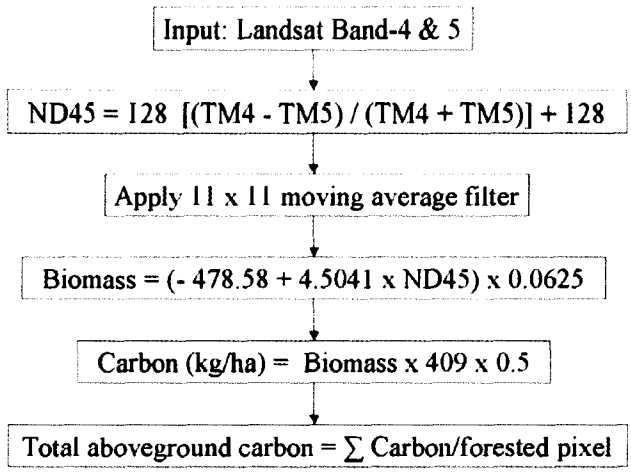

Figure 9. Landsat aboveground carbon computing procedure

The program computes ND45 over forested areas. An 11x11 average filter is applied to ND45 to reduce noise in a Landsat image. Next, biomass volume in m3/pixel is calculated. Because the spatial resolution of Landsat imagery is 25 meters, 0.0625 is used convert the pixel area to hectares. Based on the Landsat biomass, Landsat aboveground carbon for each forest pixel is computed.

4.8 Afforestation, Reforestation, and Deforestation Calculations

Article 3.3 of the Kyoto Protocol specifies that "the net changes in greenhouse gas emissions by sources and removals by sinks resulting from direct human-induced land-use change and forestry activities, limited to afforestation, reforestation and deforestation since 1990, measured as verifiable changes in carbon stocks in each commitment period, shall be used to meet the commitments under this Article of each Party" [41]. To support

this Article, KAPCS has an ARD unit to compute afforestation, reforestation and deforestation from multitemporal remote sensing classification images.

The ARD definitions defined by the Intergovernmental Panel on Climate Change (IPCC) [41] are as follow:

"Afforestation (A) is the direct human-induced activities of planting new forests on the lands that, historically, have not contained forests. Reforestation (R) is the direct human-induced activities of planting forests on lands that have, historically, previously contained forests but that have been converted to non-forest land. Deforestation (D) is the direct human-induced conversion of forested land to non-forested land."

When multitemporal remote sensing images are used for ARD estimations, the remote sensing ARD definitions are slightly different from the ARD definitions set by IPCC. In the multitemporal remote sensing analysis of this thesis, the earliest date of the image is set as the base image. The land use before the base year was unknown. Therefore, the remote sensing afforestation is that new forests in the later remote sensing images are detected on the non-forested lands in the base image. The remote sensing reforestation is that the planting of forests on lands that have been clear-cut areas in the early-date remote sensing images. The remote sensing deforestation is that forested lands in the early-date images are converted to the non-forested lands, on which there is no reforestation detected in the later remote sensing images.

Based on these ARD definitions, classes in the classification images are converted into four basic land-type classes: Forest, Non-Forest, Regeneration, and Unclassified. The forest class contains Softwood, Hardwood, and Mixed wood. The unclassified class

consists of unclassified pixels, no-data areas, clouds and cloud shadow. The regeneration class refers to young trees. All of the other classes are set to the no-forest class.

ARD	Year 1	Year 2	Year 3
Afforestation Year 2	Non-Forest	Forest	Forest
Afforestation Year 2	Non-Forest	Forest	Regeneration
Afforestation Year 2	Non-Forest	Regeneration	Forest
Afforestation Year 2	Non-Forest	Regeneration	Regeneration
Afforestation Year 3	Non-Forest	Non-Forest	Forest
Afforestation Year 3	Non-Forest	Non-Forest	Regeneration
Reforestation Year 2	Forest	Regeneration	Forest
Reforestation Year 2	Forest	Regeneration	Regeneration
Reforestation Year 3	Forest	Forest	Regeneration
Reforestation Year 3	Forest	Non-Forest	Forest
Reforestation Year 3	Forest	Non-Forest	Regeneration
Reforestation Year 3	Regeneration	Non-Forest	Forest
Reforestation Year 3	Regeneration	Non-Forest	Regeneration
Deforestation Year 2	Forest	Non-Forest	Non-Forest
Deforestation Year 2	Regeneration	Non-Forest	Non-Forest
Deforestation Year 3	Forest	Forest	Non-Forest
Deforestation Year 3	Forest	Regeneration	Non-Forest
Deforestation Year 3	Regeneration	Forest	Non-Forest
Deforestation Year 3	Regeneration	Regeneration	Non-Forest
Forest	Forest	Forest	Forest
Forest	Regeneration	Forest	Forest
Forest	Regeneration	Forest	Regeneration
Forest	Regeneration	Regeneration	Forest
Forest	Regeneration	Regeneration	Regeneration
Non-Forest	Non-Forest	Forest	Non-Forest
Non-Forest	Non-Forest	Non-Forest	Non-Forest
Non-Forest	Non-Forest	Regeneration	Non-Forest

Table 3. Afforestation, Reforestation, and Deforestation permutation table

An ARD permutation table is then used to convert the basic land types to the ARD classes [8]. *Table 3* shows the twenty-seven permutations of the three land-types for

three Landsat images. To avoid having too many permutations when more than three dates of Landsat images are used in a multitemporal data set, a three-date ARD sliding window is built. It computes ARD for the first three dates of the classification images and then moves it one date forward and computes the next three-date ARD image until the process finishes.

5 Software Implementation

The implementation of KPACS is developed from a mix of legacy FORTRAN modules, created by the Landsat Digital Image Analysis (LDIAS) project of the Canada Centre for Remote Sensing (CCRS), and a set of new software modules. For the legacy FORTRAN modules, VAX FORTRAN code was converted to FORTRAN-77 code, integrated with the PCI Geomatica libraries, and compiled on the Solaris UNIX operating system. The required new modules were designed, implemented, and integrated with the other modules to form KPACS.

5.1 Legacy FORTRAN Modules

In the mid 1980's, a large software and hardware system for processing Landsat TM data, the Landsat Digital Image Analysis System (LDIAS), was created for VAX computers under the VMS operating system. It was developed by a team of scientific researchers, led by Dr. David Goodenough at the Canada Centre for Remote Sensing (CCRS). The entire program consisted of 1.5 million lines of VAX FORTRAN code. In 1995, parts of the legacy FORTRAN code, image segmentation and classification, in the LDIAS package were converted to UNIX with Sun FORTRAN 77 compilers. The converted software package was renamed as the Robust Image Analysis system for Satellites and Aircraft (RIASSA) [42].

RIASSA had limitations. The package was designed to process single-date LANDSAT TM imagery. The number of spectral bands that RIASSA could handle was

restricted to sixteen. Moreover, the maximum number of segments in a segmentation image was limited to 32767. The PCI libraries integrated into RIASSA were from an earlier version of the Geomatica PCI package that was not compatible with the current version of the PCI software.

To meet the requirements of KPACS, five tasks needed to be conducted. Task one was to implement the Feature Selection [33] module. Task two was to enhance the KPACS segmentation ability to handle more than 32767 segments than RIASSA. Task three was to expand the number of input spectral bands allowed by RIASSA. Task four was to update the earlier version of PCI libraries to the current version. Task five was to create new software modules for generating training statistics, adaptive classification, forest biomass, and aboveground carbon calculations.

5.2 Converting VAX FORTRAN Components

To convert VAX FORTRAN modules to FORTRAN-77 modules running on UNIX, one of the difficulties was to change the VAX FORTRAN's full-featured and console-based user interface to the Geomatica PCI EASI user interface. The VAX user interface was constructed by making frequent function calls to a VAX-specific library, Man-Machine Interface Library (MMILIB) in LDIAS. The conversion needed to replace the MMLIB function calls and subroutines with PCI or RIASSA function calls. Another difficulty was that the file I/O routines in VAX FORTRAN needed to be replaced with PCI or FORTRAN-77 I/O routines. *Table 4* is the summary of the one-to-one relations between the MMILIB function calls and the PCI/RIASSA/FORTRAN-77 library calls.

MMILIB Calls	PCI/FORTRAN/RIASSA	Function Purpose
MMGETLUN	LUNGET (FORTRAN)	Get unit number for a file
MMWRTERR	WRITE (FORTRAN)	Write an error message
MMWRTLIN	WRITE (FORTRAN)	Write a line
MMASKI4	IMPSTS (PCI)	Provide interface for getting parameters
MMDSPTXT	IMPPRB (PCI)	Prompt user and read response
MMYESORNO	IMPPRC (PCI)	Prompt user for a single character
MMMENU	IMPPUI (PCI)	Prompt user for an Integer
MMTRUDEF	DEFTRU (RIASSA)	Determine if TRUTH file exists
MMSTIDEF	DEFSEG (RIASSA)	Determine if STATISTICS file exists
DKOPEN	TXTOPN (PCI)	Open a disk file
DKCLOS	TXTCLS (PCI)	Close disk file
DKWRIT	WRITE (FORTRAN)	Write to disk file
DK4SET	Not used	Specify next block to write
DKWAIT	Not used	Wait for completion
DKREAD	READ (FORTRAN)	Read from a disk file
DLDLET	TXTOPN (PCI)	Delete disk file

Table 4. MMILIB Functions replaced by PCI / RIASSA / FORTRAN functions

There were also incompatibilities in intrinsic functions between VAX FORTRAN and FORTRAN-77. Even though most of the non-standard intrinsic routines in VAX FORTRAN on the VMS operating system were recognized by FORTRAN-77, such as TIME (Current time) and JZEXT (Zero-extend), there were still a few of VAX intrinsic functions, which were not supported by FORTRAN-77.

For example, the function RAN() that produced a sequence of random numbers with a uniform distribution is one of them. To convert the incompatible intrinsic functions such as RAN(), new codes were written. *Table 5* shows the replacement of the intrinsic function RAN(). TIMEARRAY returns the hour, minute and second of the day, which are used as the different seeds for the new function RAND in FORTRAN-77 to generate random numbers with uniform distribution.

Original VAX FORTRAN code:	Converted FORTRAN-77 code:

AC = 0.
  DO I = 1, 27
  AC = AC + RAN (SEED)
ENDDO
	DO I = 1, 27
	  CALL ITIME(TIMEARRAY)
	  AC = AC + RAND(TIMEARRAY (1) +
	  TIMEARRAY (2)+ TIMEARRAY (3))
	ENDDO

Table 5. VMS RAN function and FORTRAN-77 RAND function

5.3 Increasing the Number of Segments

The LDIAS was implemented in the mid 1980's. At that time memory cost was a significant concern. As the result, most of integer types in the LDIAS programs were declared as a two-byte signed integer ranging from -32767 to +32767. Even though the segmentation and classification modules of LDIAS had been converted to UNIX and become part of RIASSA, the integer types in the programs were not changed. Consequently, the maximum number of segments in a segmentation image was still limited to 32767. This limitation created a bottleneck when the modules were used to process multitemporal Landsat imagery, because the more Landsat images added to the multitemporal data set, the larger number of segment objects generated in a segmentation image. The total number of the segments may exceed 32767.

Simply changing all of the integer types from the two-byte integer to the four-byte integer (32 bits) was not an efficient solution. In LDIAS and RIASSA, the configuration of data passing between software modules relied on files. Even within a module itself, intermediate files were widely used to store temporary results. Because the FORTRAN file system is record-oriented and records in a file are organized as sequences of bytes in blocks, the file block numbers and byte offsets in LDIAS and RIASSA were constructed

precisely based on a record length. If the integer types in a module were redefined from the two-byte integer to the four-byte integer, the file structure used by the module had to be redefined. Moreover, other modules having access to this file had to be updated as well. This conversion became more complex and more coding changes were required, which might also increase chances of introducing errors into the previous coding.

The approach in the KPACS implementation to this problem was to trace variables that cause the limitation on the number of the segments in a segmentation image. The first variable was the segment counter that records the total number of segments in the segmentation image. It was stored in the first block of the statistics file and shared by other modules in KPACS. After changing this variable to the four-byte integer, its record length in the first block of the statistics file was modified to match this change. The following modifications then concentrated on the modules or subroutines, which required accessing the segment counter variable in the statistics file.

The second variable required to be updated from the two-byte integer type to the four-byte integer type was the block-counter variable that records the total number of data blocks in the statistics file. Since the number of elements in a covariance matrix increased in quadratic order with the number of input multispectral bands, the total number of blocks in the statistics file might exceed 32767, especially when working with multitemporal Landsat images. The procedure of changing the block-counter variable from the two-byte integer to the four-byte integer was similar to the procedure of updating the segment-counter variable.

When the integer type of the block-counter variable was changed to four bytes, the statistics file was restructured to accommodate this change. The rest of modifications were then moved to the modules or subroutines that required accessing the statistics file.

5.4 Increasing the Number of Input Channels

The LDIAS or RIASSA programs were developed to process a single-date LANDSAT image with six multispectral bands. Subsequently, the maximum number of input bands allowed by RIASSA was sixteen. To meet the requirements of KPACS and to be able to process multitemporal Landsat data set containing more than one of Landsat images, the maximum number of input channels was increased.

The maximum number of the input channels could not be increased too high without considering the Hughes problem [43]. When the total number of input channels increases, the number of training samples needed to adequately define the classes quantitatively, regardless of what classification methods are used, grows very rapidly [44]. Thus, allowing too many input channels might either decrease the classification accuracy or cause the training collection to become too expensive.

In KPACS, the total number of input multispectral channels was increased from sixteen to thirty-two. In the LDIAS or RIASSA system, there was no static global variable for holding the value of the maximum number of input bands allowed by the system. So, the modification included creating a new global variable, searching for the old settings, and replacing them with the new global variable. When the maximum

number of input channels was increased, the total number of elements allowed in a covariance matrix by KPACS was also updated.

5.5 Working with the New Version of PCI Libraries

KPACS was designed to be a plug-in module of the Geomatica PCI EASI/PACE Image Analysis System on UNIX. Therefore, the KPACS programs used a large number of the PCI library function calls to build the user interface, ingesting/creating remote sensing images, and carrying out other I/O operations.

In the previous conversion of the segmentation and classification programs in the RIASSA system, the PCI function calls were implemented with an earlier version of PCI library that was no longer compatible with the newer version of the PCI libraries. To incorporate the segmentation and classification modules into KPACS, the old version of the PCI libraries were replaced with the new version of the PCI libraries.

There were several problems for this upgrade. First, the names of the PCI libraries in the new version were different from the previous ones. To link to the new PCI libraries, the changes on library names had to be made in Makefile. There were two PCI libraries required by KPACS. One was the static library, and the other was the dynamic library. In the old version of PCI, the static library was called "pcilib.a", and the dynamic library was called "pcilibf.a". In the new version, the former was changed to "pci.a", and the latter to "pcif.a".

Secondly, the FORTRAN compiler used to link the PCI libraries had to be switched from the SUN FORTRAN-77 compiler to the GNU FORTRAN compiler. The

former has abilities to tolerate a few non-standard VAX intrinsic functions, but the latter not. Thus, the non-standard FORTRAN-77 statements in the previous software modules were converted to the standard FORTRAN-77 language. Most of the VAX statements could be replaced with the corresponding standard FORTRAN-77 code. Examples are shown in *Table 6.*

Unsupported VAX Statement	Standard FORTRAN-77 Statement
TYPE LINE, L	**WRITE** (TTYOUT, LINE) L
FORMAT(X, **I**)	FORMAT(**1**X, **I4**)
CALL **DATE**(C_DATE)	CALL **FDATE**(C_DATE)
IF (INTEGER .EQ. **'N'**) THEN	IF (INTEGER .EQ. 0) THE
FORMAT(1X, 'Level: ' 7(I8))	FORMAT(1X, 'Level: ', 7(I8))
BYTE CLASS_NAME**(16)** DO J = 1, 16 CLASS_NAME(J) = ' ' ENDDO	**CHARACTER*16** CLASS_NAME CLASS_NAME = ' '
JMOD (J_SETS, J_MAX)	**MOD** (J_SETS, J_MAX)
JSMPLS = **JZEXT**(IBUF(K))	JSMPLS = IBUF(K)
INTEGER*4 C**$**_PIX, C**$**_LINE, C**$**_CHAN	INTEGER*4 C_PIX, C_LINE, C_CHAN
ENCODE(60,20,TERSE(1)) FEAT_NUM	**WRITE**(TERSE(1),20) FEAT_NUM
FORMAT(A, **F**)	FORMAT(A, **F10.2**)
AC = AC + **RAN**(SEED)	AC = AC + **RAND**(SEED)

Table 6. Non-standard VAX FORTRAN conversion

Finally, variable initializations were required by the GNU FORTRAN compiler. In previous LDIAS and RIASSA programs, most of global and local variables were not initialized. The un-initialized variables were initialized with the default values by the SUN FORTRAN-77 compilers. But the GNU FORTRAN compiler did not assign default values to these un-initialized variables. The un-initialized variables either contained arbitrary values or caused program executions to terminate or abort.

Variables not initialized	Variables initialized
Class 2 Number of pixels = 30367. Number of segments =********** Average size = 0. Pixels Standard deviation = 0. Pixels Average of the means: 0.000 0.000 0.000 0.000 0.000 0.000	Class 2 Number of pixels = 30367. Number of segments = 1239. Average size = 25. Pixels Standard deviation = 18. Pixels Average of the means: 71.031 58.600 57.420 80.842 103.041 60.646

Table 7. Errors caused by un-initialized variables

Table 7 shows an example of the initialization problem. On the left hand of the table, the variables were not initialized. The variable containing the number of segments overflowed and the mean vector had zero values. On the right hand of the table, the variables were initialized and they had the correct values. As the part of system modification, all global variables were initialized.

6 Image Processing and Research Results

Four Landsat images of the Hinton study area were used to test the KPACS performance. The four dates of the Landsat images were 1985, 1990, 1996 Landsat TM image, and 2001 Landsat ETM+ image. Before these images were fused for the multitemporal segmentation, classification, carbon estimates, and ARD analysis, pre-processing of the multitemporal Landsat images was required. The steps in the preprocessing of the Landsat images included radiometric correction and geometric correction.

6.1 Multitemporal Landsat Imagery Acquisition

Four different dates of LANDSAT TM images were collected between 1985 and 2001. Three of them were acquired from LANDSAT-5 TM, and one from LANDSAT-7 ETM+. *Table 8* shows the Landsat imagery collection information.

Satellite	Sensor	Path	Row	Date	Cloud % (in 24 TWR)
Landsat-5	TM	45	23	07/31/1985	5% (0.1%)
Landsat-5	TM	45	23	07/29/1990	5% (2.8%)
Landsat-5	TM	45	23	07/13/1996	10% (2.6%)
Landsat-7	ETM+	45	23	07/03/2001	10% (3.4%)

Table 8. Landsat TM and ETM+ imagery acquisitions

A typical growing season in the forested regions of Canada commences in April and concludes in October. In order to minimize radiometric differences and vegetation changes between images, Landsat data were acquired during the peak-growing month of

July. Data acquired for use in this study were selected to minimize the effects of vegetation growth.

The Landsat TM images had been geo-corrected (orthorectified) through the previous studies [8, 36]. The orthorectification process of the 1985 Landsat-5 TM image used seventeen ground control points (GCPs) and the digital elevation model (DEM) created from sixteen 1:20000 digital NAD'83 topographic files that were provided by the Province of Alberta. The Alberta-base road vector was used to assess the resulting accuracies of the geometric correction. The 1990 and 1996 Landsat-5 TM images were provided by RADARSAT International (RSI) and geo-corrected. A correction for topographic relief was applied with a 64-point $[\sin(x)/x]^2$ resampling kernel. The spatial resolution of all three Landsat TM images was resampled to 25 metres. Image-to-image registration to the 1985 Landsat-5 TM image was also performed on the 1990 and 1996 Landsat-5 TM images with a 16 point $[\sin(x)/x]^2$ resampling kernel. The root-mean-square (rms) error was 0.46 pixels for the 1990 Landsat-5 TM image and the rms error 0.49 for the 1996 Landsat-5 TM image. Data fusion for these three-date Landsat-5 TM images was better than 0.5 pixels.

The 2001 Landsat-7 ETM+ image was acquired from the Centre for Topographic Information (CTI), Natural Resources Canada, for this study. Before the Landsat-7 ETM+ image was fused into the multitemporal Landsat TM data set, geometric correction and image-to-image registration were performed. *Figure 10* (a) shows the uncorrected Landsat-7 image and *Figure 10* (b) the associated metadata table.

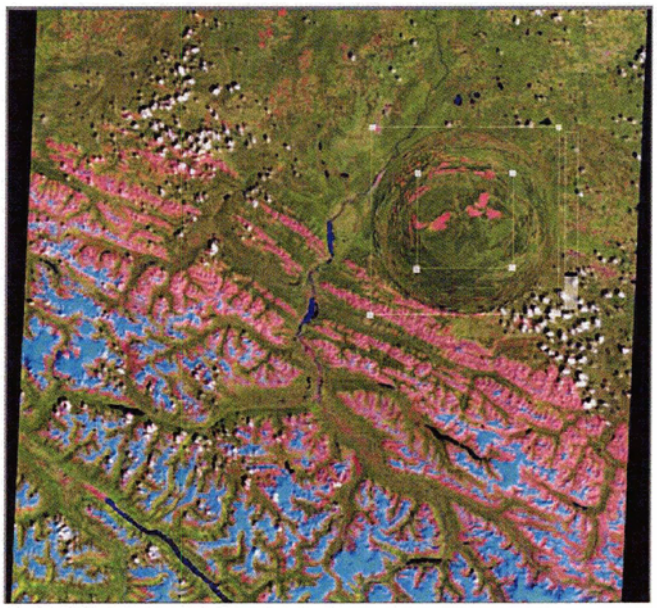

PARAMETERS	
Satellite:	*7*
Sensor:	*ETM+*
P/R:	*45/23*
Cyc:	*51*
AOS&LOS:	*183008 184205*
RevNum:	*11798*
Date:	*2001-JUL-03 18:37:01*
Center:	*53°06'00"N, 117°55'23"W*
Cloud:	*1111*
% cloud:	*10*
Statn:	*PASS*
Hdtid:	*PA420093*
Top Left	*54°05'16"N, 118°54'41"W*
Lower Right	*52°06'11"N, 116°58'59"W*
Scene Time:	*2001-JUL-03:18:37:01.184*

(a) Uncorrected ETM+ image (b) Meta data table

Figure 10. Uncorrected Landsat-7 ETM+ image and associated metadata

The spatial resolution of the original Landsat-7 ETM+ image was 30 metres. A zoom-in area in *Figure 10* (a) illustrates a small portion of detailed land cover in the Hinton study site. The band combination for displaying the image is Band-5, 4, and 3. The metadata in *Figure 10* (b) provides the most important information about this Landsat-7 ETM+ image, such as satellite: Landsat-7, sensor: ETM+, Path/Row: 45/23, acquisition date: July 3, 2003, acquisition time: 18:37:01, scene centre: 53°06'00"N - 117°55'23"W, cloud coverage: 10%, top of left corner of the image: 54°05'16"N - 118°54'41"W, and lower right corner of the image: 52°06'11"N, 116°58'59"W.

6.2 Orthorectification of Landsat-7 ETM+ Image

The geometric correction was performed on the Landsat-7 ETM+ image with the PCI Geomatica™ OrthoEngine. OrthoEngine was started up by running "orthoeng" from the Unix command prompt. Under File/New in OrthoEngine, a Landsat-7 image project was created with the Satellite Orbital Modeling and Landsat Options selected. Output Projections was set to be UTM Zone 11 for the Hinton area and Earth Model to be NAD83. The GCP projections were based on the output projection. The raw Landsat-7 ETM+ image was then loaded into OrthoEngine.

The DEM file required by OrthoEngine was the same DEM file as used for orthorectifying Landsat TM images. The spatial resolution of the DEM was 25 metres. The Alberta-base road vector was used for collecting the GCPs in OrthoEngine. A location on the Alberta-base road vector was selected first, and then the same point on the 2001 Landsat-7 ETM+ image. In the GCP Selection and Editing window of OrthoEngine, this location was accepted as a GCP. After three GCPs had been taken, any further GCP points selected from the Alberta-base road vector would appear in the uncorrected Landsat-7 image as well. The GCPs should cover as much area as possible and spread out evenly over the entire image. One useful method in OrthoEngine for checking errors in GCPs was to turn each GCP into a Check Point. If the RMS error of the GCPs decreased drastically, this GCP point was likely mislocated. Therefore, it was either relocated, or changed to a Check Point. Check Points would not be included in the registration model computation.

Twelve ground control points (GCPs) and three check points were selected. *Table 9* shows the detailed GCP information. The column, Point ID, in *Table 9* lists all of the GCPs registered. If a Point ID is negative, for example "–15", this Point ID is a Check Point. The column, Res, lists the residual errors for the GCPs. The column Res X and ResY show residual errors in X directions and Y directions.

Point ID	Res	Res X	Res Y	Type
-15	0.75	-0.71	0.26	Check
2	0.44	0.16	0.41	GCP
9	0.34	-0.18	-0.29	GCP
5	0.33	0.02	-0.33	GCP
1	0.26	-0.01	-0.26	GCP
4	0.25	0.07	0.24	GCP
3	0.24	-0.01	0.24	GCP
-14	0.20	0.14	0.13	Check
-13	0.14	0.14	0.03	Check
10	0.11	-0.02	0.11	GCP
8	0.10	0.01	-0.10	GCP
7	0.09	-0.09	-0.02	GCP
11	0.06	-0.02	0.06	GCP
12	0.06	0.02	-0.05	GCP
6	0.04	0.04	-0.02	GCP

Table 9. GCP-list report of geometric correction for the 2001 Landsat image

The orthorectified Landsat-7 ETM+ image was resampled to the 25-metre spatial resolution with a 16-point $[\sin(x)/x]^2$ function resampling kernel. The rms errors for orthorectifying the 2001 Landsat-7 ETM+ image were 2 m in the X direction and 5.8 m in the Y direction.

To make the 2001 Landsat-7 ETM+ image match the Landsat-5 TM imagery geometrically with minimum errors, the OrthoEngine-corrected Landsat-7 ETM+ image was registered to the base reference of the 1985 Landsat-5 TM image with PCI Geomatica™ GCPWorks. In GCPWorks, the Thin Plate Spline was selected as the mathematical model. The OrthoEngine-corrected Landsat-7 ETM+ image was loaded

into GCPWorks as an uncorrected image. The Alberta-based road vector was overlaid on top of the 1985 Landsat-5 TM image and used as the Source of GCPs in GCPWorks.

After three GCPs were collected, the vector file was also overlaid on the 2001 Landsat-7 ETM+ image. In the next step, the accurate GCPs were established by inversely rubber sheeting the Alberta-based road vectors to fit the Landsat images [45]. *Figure 11* illustrates an example. In *Figure 11* (a), the road vector was overlaid on the 1985 Landsat-5 image. In *Figure 11* (b), the same road vector was placed on top on the Landsat-7 ETM+ image. By adjusting the position of the road intersection in *Figure 11* (b), the GCP at this road intersection matched the same GCP location in *Figure 11* (a).

(a) 1985 Base Image (b) 2001 Landsat-7 Image

Figure 11. GCP adjustments in the image-to-image registration

The image-to-image registration was performed on the 2001 Landsat-7 ETM+ image with a 16 by 16 $[\sin(x)/x]^2$ resampling function. The rms error of the registration process was 0.45 pixels for the 2001 Landsat-7 ETM+ image, which was now ready to be fused into the Landsat-5 TM data set.

6.3 Radiometric Correction

Because of the lack of ground radiometric measurements at the time of acquisitions, no atmospheric correction was performed on the Landsat images. To reduce the radiometric differences between different Landsat images, radiometric normalizations were applied. As with the image registration, the reference image was set to the 1985 Landsat TM image.

Radiometric comparisons between the 1985 Landsat TM image and other Landsat images were performed. Due to no significant difference in the radiometry between the 1985 and 1996 Landsat TM images, the radiometric normalizations were only carried out for the 1990 and 2001 Landsat images.

The radiometric regression relationships between the 1985 and 1990 Landsat images and the 1985 and 2001 Landsat images were developed. *Figure 12* shows these radiometric normalization relationships for bands 4 and 5. The 2-D scatter plots demonstrate the pixel distributions and correlations between the two dates. Band 4 (or 5) from the reference image (1985 Landsat TM) was used as the y-axis, and Band-4 (or 5) from the 1990 or 2001 image was used as the x-axis. To obtain the correct linear regression functions, pixels that had changed (i.e. that had no correlations between the multitemporal Landsat images) were removed using a "no-change" mask (see section 6.4). *Figure 12* (a) shows the scatter-plot diagrams for Band 4, and *Figure 12* (b) shows the scatter plot diagrams for Band 5.

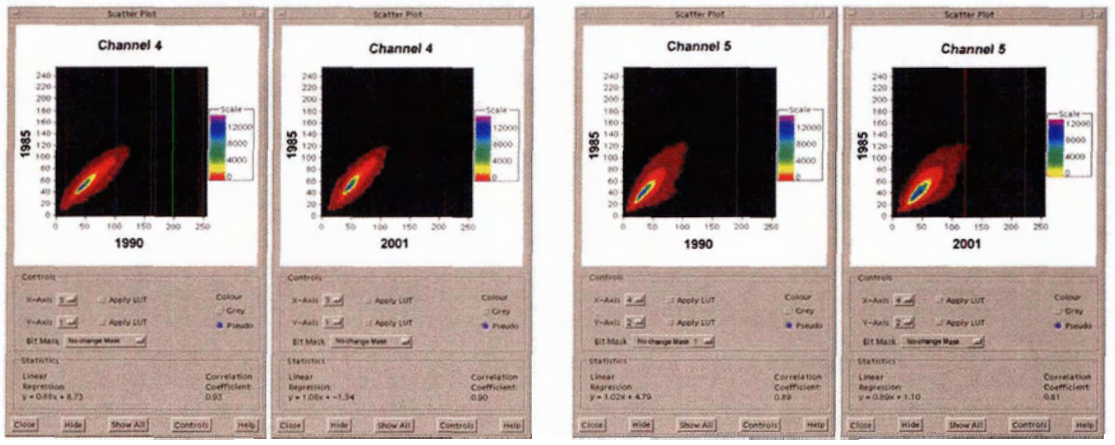

(a) Scatter plots for Band 4 for 1990 and 2001 compared to 1985 reference

(b) Scatter plots for Band 5 for 1990 and 2001 compared to 1985 reference

Figure 12. Scatter plot images and correlation relationship functions

The radiometric relationship functions for Landsat Band 4 of the 1990 and 2001 normalization were (9) and (10) respectively.

$$1985\_Channel\_4 = 0.88 \times 1990\_Channel\_4 + 8.73 \quad (9)$$

$$1985\_Channel\_4 = 1.08 \times 2001\_Channel\_4 - 1.34 \quad (10)$$

The radiometric relationship functions for Landsat Band 5 of the 1990 and 2001 normalization were (11) and (12) respectively.

$$1985\_Channel\_5 = 1.02 \times 1990\_Channel\_5 + 4.79 \quad (11)$$

$$1985\_Channel\_5 = 0.89 \times 2001\_Channel\_5 + 1.10 \quad (12)$$

By applying these radiometric relationship functions, bands 4 and 5 of the 1990 and 2001 Landsat images were linearly transformed to the 1985 Landsat TM image (the reference image).

6.4 No-Change Mask

A no-change mask covering the Hinton study site was created. This mask shows the areas, where no-change has occurred since 1985. There were several steps to generate the no-change mask. The first step was to identify three sample target areas: dark water (dark target), airport runway (bright target) and Pine forest area (mid level). The radiometry means of the sample areas were calculated in each spectral band, and the measurements were then plotted onto a 2-D plane. *Figure 13* gives an example of the scatter plots derived from these three sample areas. In *Figure 13* (a), the 2-D scatter plot shows the sample-mean distributions between the 1985 Landsat-5 TM image and the 2001 Landsat-7 ETM+ image with Band 3 from the 1985 image as the y-axis and Band-3 from the 2001 image as the x-axis. *Figure 13* (b) is the scatter plot for Band 4. The same process was applied to all spectral bands in the multitemporal Landsat image.

The next step was to choose the spectral bands that had the ability to separate the three identified targets from each other for generating a no-change mask. From the example illustrated in *Figure 13*, clearly Band 4 was better than Band 3 because Band 3 would have difficulty to separate dark water and Pine forest. Through the comparison between all of the spectral bands, bands 4 and 5 were selected in this thesis for creating the no-change mask.

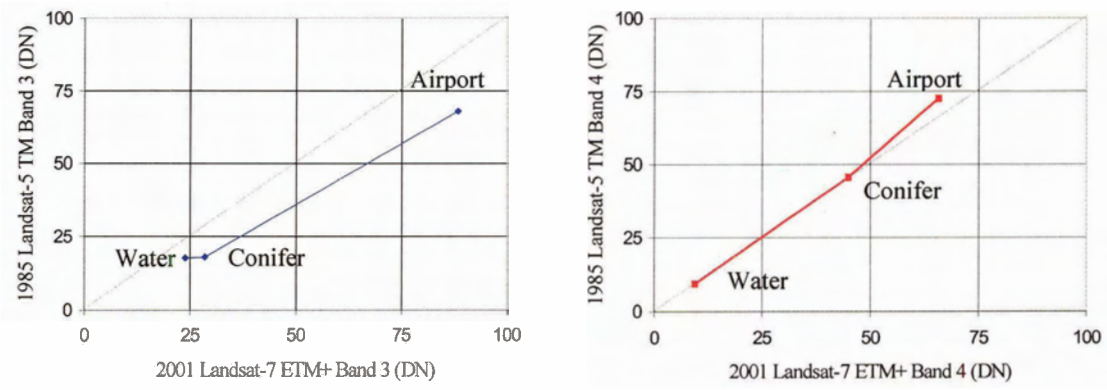

(a) Scatter plot for Band 3 between the 1985 and 2001 images based on digital numbers.

(b) Scatter plot for Band 4 between the 1985 and 2001 images based on digital numbers.

Figure 13. Scatter plots for three sample areas

Before the no-change mask creation, a 5×5 average filter was applied to bands 4 and 5 on all Landsat images to eliminate noise. Then, the maximum difference of DN values in a pixel was calculated with the function (13). The result was saved to a new image band.

$$oc = \underset{i=1}{\overset{4}{MAX}} | ic[i] | - \underset{i=1}{\overset{4}{MIN}} | ic[i] | \qquad (13)$$

where oc is an output channel containing the "maximum-difference" image; ic is the input channel: Band 4 or 5. i represents the four dates Landsat images from 1985 to 2001. Two maximum-difference images were generated: one from Band 4 and the other from Band 5.

The final step was to select threshold values in the two maximum-difference images to exclude pixels that had the difference values larger than the thresholds. The

threshold values were decided through the Histograms of the two images. *Figure 14* shows a histogram of the maximum-difference image derived from Band 4.

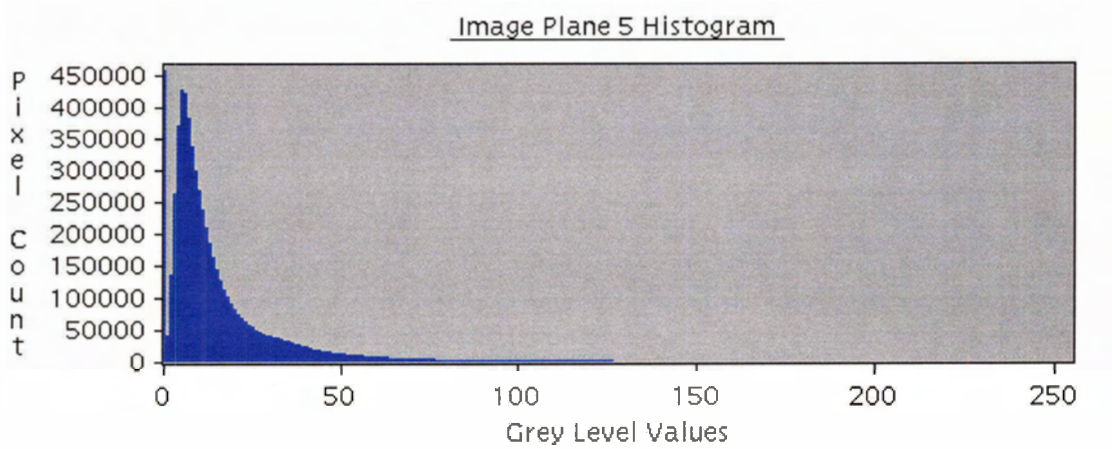

Figure 14. Histogram of the maximum-difference image from Band 4

To set the proper thresholds, several trials were needed by checking the pixels, which had the grey level value being the same as the threshold value, between the four-date Landsat images. If the threshold values were too large some of "changed" pixels would have been included in the no-change mask. On the other hand, if the threshold values were too small some of the "unchanged" pixels would have been missed when generating the no-change mask. In this research, the threshold value for Band 4 was set to 12, and the threshold value for the band-5 was set to 23.

If a pixel in the Band 4 maximum-difference image had a grey level value less than or equal to the Band 4 threshold value and the same pixel in the Band 5 maximum-difference image had a grey level value less than or equal to the Band 5 threshold value, this pixel was included in the no-change mask.

6.5 Data Fusion

When the image pre-processing was finished, the geometrically corrected and radiometrically corrected Landsat images from 1985, 1990, 1996 and 2001 were fused into one multitemporal data set that was ready for the image segmentation process. Because the Landsat imagery covering the entire Hinton study area has 3360× 1880 pixels, which is too large for the KPACS software to process at one time, the fused Landsat data set was subsetted into seven image tiles, each of which covers an area of 1024× 1024 pixels. *Figure 15* shows an example of a subsetted data cube of Tile D from the Landsat imagery of 1985, 1990, 1996 and 2001 acquisitions. The image at the bottom of *Figure 15* is the 1985 Landsat-5 TM image. On top of it are the 1990 and 1996 Landsat-5 TM images respectively. The 2001 Landsat-7 ETM+ image is on the top. The UTM coordinates for each image tile are listed in *Table 10*.

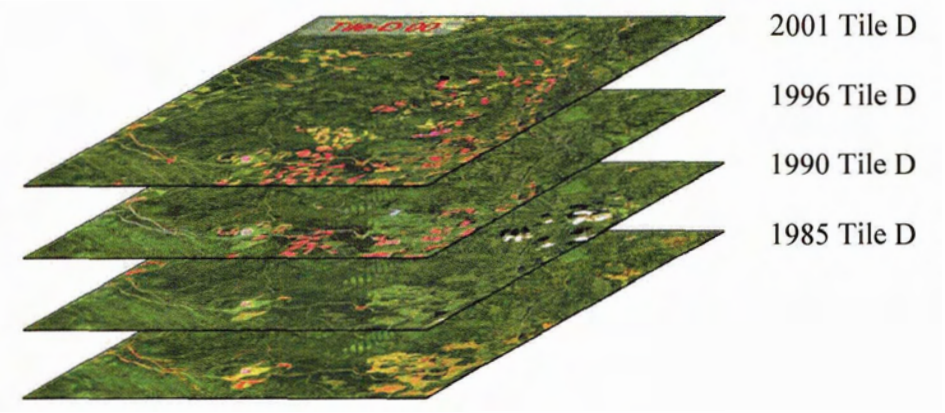

Figure 15. Landsat TM data fusion for Tile D of Hinton

	Upper Left	Upper Left	Lower Right	Lower Right
Tiles	Easting	Northing	Easting	Northing
Tile A	443000	5917000	468600	5891400
Tile B	462275	5917000	487875	5891400
Tile C	481925	5917000	507525	5891400
Tile D	501400	5917000	527000	5891400
Tile E	457275	5895600	482875	5870000
Tile F	479425	5895600	505025	5870000

Table 10. Tile coordinates and number of segments in each tile

6.6 Multitemporal Image Segmentation Process

Image segmentation on the fused Landsat data set was a process to group adjacent pixels based on their intensity values to create homogeneous segments in the imagery. The segment objects were then used in the later classification process. The homogeneous level of smoothness of a segment was controlled by a threshold parameter. The detailed segmentation algorithm can be found in 4.2 Image Segmentation.

Multitemporal classification requires consistent segment boundaries for change detection and comparison. Therefore, the segmentation process should be performed on fused Landsat imagery rather than on each individual image. There are two ways to segment a multitemporal image. First, if the number of spectral bands in the multitemporal data set is less than the KPACS limit (current limit: 32), the consistent segment boundaries can be obtained by segmenting the entire fused data cube. Secondly, if the number of spectral bands in the multitemporal data set exceeds the KPACS limit, Feature Selection should be performed to reduce the number of input channels (See 6.8) before the segmentation process can be used.

The fused Landsat data cube in this research had twenty-four multispectral bands collected from the four dates of the Landsat images, which were acceptable by KPACS for segmentation. By adjusting the optimization parameter to 120 the optimal segmentation results were achieved. The total numbers of segments in each image tile are shown in *Table 11*.

Tiles	Tile A	Tile B	Tile C	Tile D	Tile E	Tile F	Tile G
Number of Segments	26644	30426	28962	29095	30372	26626	28945

Table 11. Number of segments in image tiles

If the optimization threshold was less than 120, more small size segments would have been created that might lead to poor classification results since those small segments did not have enough pixels to produce valid statistics when a Gaussian classifier was used and might increase the processing time for image segmentation and classification. However, if this threshold value were higher than 120, a segment might have covered different areas in one segment and led to poor classification results as well. *Figure 16* shows an example of a small portion of the segmentation boundaries overlaid on top of the 1990 Landsat-5 TM image (a) and the 1996 Landsat-5 TM image (b).

When more dates of Landsat images are added in to an existing multitemporal data cube, more segments will be generated because of changes that occurred in the later images. The optimization threshold parameter should be adjusted and checked each time when a new data cube is formed and segmented.

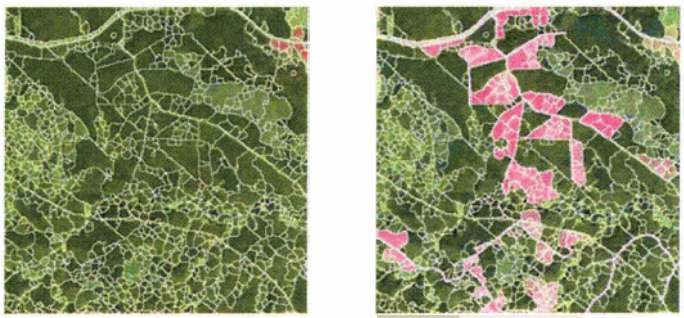

(a) Segments in 1990 Landsat-5 TM image (b) Segments in 1996 Landsat-5 TM image

Figure 16. Example of segmented multitemporal Landsat images

6.7 Training Areas Identification

The ground training information was obtained from a set of the forest inventory maps [46] provided by the Resource Evaluation and Planning Division of the Alberta Forest Service. These maps provide major vegetation forest types based on polygons. These polygons may roughly be compared to the segment boundaries in the segmentation image. The information in the maps included the forested land, non-forested land, forest crown density, forest composition and clear-cut areas. The map was updated in March of 1993 and the photo scale used was 1:40000.

Twenty-three training classes were identified from the forest cover maps. The three major forest types were coniferous, deciduous, and mixed wood. The coniferous class contained at least 80% conifer and no more than 20% deciduous. The deciduous class had at least 80% deciduous and no more than 20% coniferous. All other forest types were labelled as mixed wood.

The last update of the forest inventory map was in March of 1993. The training areas selected based on these map sheets might contain incorrect information due to the

land cover changes since 1993. A clustering technique, PCI Geomatica™ Kclus, was used to identify inhomogeneous areas or clusters. Erroneous clusters were discarded and class clusters were kept.

Kclus performed unsupervised clustering using the K-means algorithm on the training areas for a class. The output was a theme map containing the training clusters for the class in a new image channel. The number of cluster centres desired specified in the Kclus program was eight, and the maximum number of iterations in calculating the cluster mean positions was twenty. Kclus generated a statistics report of cluster mean values and sample counts after each iteration.

By analyzing the signatures of newly generated clusters of the class based on the Kclus report and the original Landsat images, clusters that did not belong to the class of interest were rejected. Similar clusters were merged. Large clusters remained as the subclasses. The new training channel created by Kclus was used for the supervised classification in 6.9. The classification results from these training clusters were then aggregated to the original training classes.

To eliminate the bias for selecting training samples, the sample points were selected systematically at equally spaced intervals over the entire study area. More than 250 training segments were identified. The number of training samples in each training class was much larger than the number of multispectral bands in the four-date multitemporal Landsat data cube, which was 32, to avoid the small training sample problem [18]. *Table 12* shows the training classes and the number of training pixels in each training class.

Class Number	Class Name	Number of Pixels
1	Conifer	146387
5	Mixed Wood	2257
6	Regeneration	3748
7	Clearcut 1985	8140
8	Clearcut 1990	6382
10	Clearcut 1996	9280
11	Clearcut 2001	8408
13	Rocks	760
16	Clear Land	163
17	Scrub Coniferous	2949
19	Scrub Deciduous	1108
26	Mine	1001
30	Water Lake (dark)	2453
31	Water River (blue)	609
32	Cloud 1985	1449
33	Cloud Shadow 1985	3031
34	Deciduous	6203
35	Cloud 1996	2449
36	Cloud Shadow 1996	3253
37	Cloud 1990	4912
38	Cloud Shadow 1990	7110
39	Cloud 2001	2712
40	Cloud Shadow 2001	2502

Table 12. Training classes and number of training pixels in each class

The training images were created for every single-date Landsat. *Figure 17* shows an example of a single-date training image created for classifying the 1985 Landsat TM image. In the training images, Coniferous is the dominant training class.

The training statistics were calculated by KPACS from all spectral bands in the data cube and saved into two KPACS files. One was the training truth file containing the training area boundary information. The other was the training statistics file containing all statistics information about the classes (See 4.4.2).

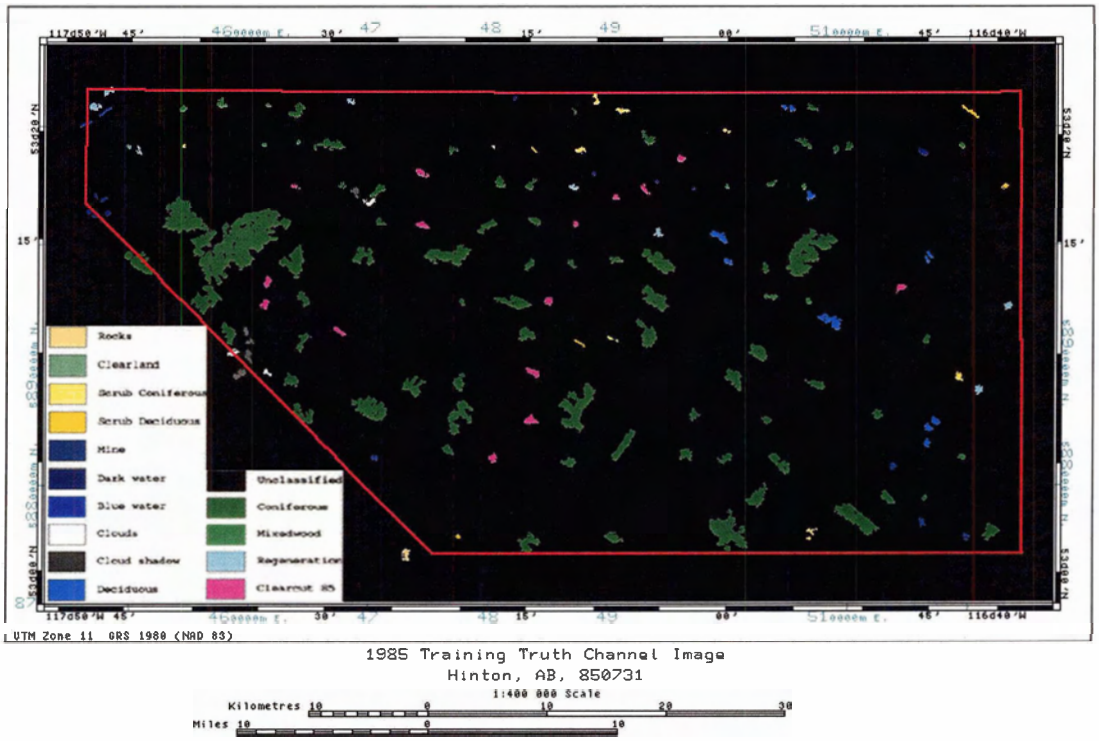

Figure 17. Training image for classifying the 1985 Landsat TM image

6.8 Feature Selection Process

KPACS is capable of processing a fused Landsat imagery with as many as thirty-two spectral bands or five six-band Landsat images. For a multitemporal Landsat imagery with more single-date images, it is necessary to perform KPACS Feature Selection to reduce the number of input channels in the fused imagery. There are two ways that a user can run Feature Selection. First, Feature Selection is run on each single-date Landsat image. The user decides how many spectral channels in a single-date image are used in the fused multitemporal data set. Then, each single-date image has the same number of spectral bands in the fused imagery. Secondly, Feature Selection is run on a fused data

set. In this way, some Landsat images may have more or less spectral channels in the fused data set than others.

Feature selection experiments in this study were conducted on the fused four-date Landsat imagery with twenty-four multispectral bands. The Landsat images were 1985 Landsat-5 TM, 1990 Landsat-5 TM, 1996 Landsat-5 TM, and 2001 Landsat-7 ETM+ image. The information about this fused data set is shown in *Table 13*.

Feature number in fused data set	Source Landsat image	Landsat band number
1	1985 Landsat-5 TM	1
2	1985 Landsat-5 TM	2
3	1985 Landsat-5 TM	3
4	1985 Landsat-5 TM	4
5	1985 Landsat-5 TM	5
6	1985 Landsat-5 TM	7
7	1990 Landsat-5 TM	1
8	1990 Landsat-5 TM	2
9	1990 Landsat-5 TM	3
10	1990 Landsat-5 TM	4
11	1990 Landsat-5 TM	5
12	1990 Landsat-5 TM	7
13	1996 Landsat-5 TM	1
14	1996 Landsat-5 TM	2
15	1996 Landsat-5 TM	3
16	1996 Landsat-5 TM	4
17	1996 Landsat-5 TM	5
18	1996 Landsat-5 TM	7
19	2001 Landsat-7 ETM+	1
20	2001 Landsat-7 ETM+	2
21	2001 Landsat-7 ETM+	3
22	2001 Landsat-7 ETM+	4
23	2001 Landsat-7 ETM+	5
24	2001 Landsat-7 ETM+	7

Table 13. Multispectral bands in the fused Landsat data set

The output features from Feature Selection were 4, 8, 12, 16, 20, and 24 features. *Table 14* shows the feature selection outputs with the optimal features in each of the

subset groups identified. Feature 1 and 6 from Band 1 and Band 7 of the 1985 image, Feature 8 from Band 2 of the 1990 image, and Feature 20 from Band 2 of the 2001 image were most important features in all twenty-four multispectral channels based on Feature Selection. The first three features appeared in all feature groups. Feature 20 was included in all feature subsets, except the feature subset containing twelve features. When the number of features in the Feature Selection output increased, Feature 4 from Band 4 of the 1985 image, Feature 7 and 12 from Band 1 and Band 7 of the 1990 image became the secondary important features in the following feature groups.

Required Number of Features	Optimal Features
4	1,6,8,20
8	1,4,6,7,8,12,14,20
12	1,2,4,6,7,8,12,13,15,18,19,24
16	1,2,4,6,7,8,9,12,13,14,15,16,18,19,20,24
20	1,2,3,4,5,6,7,8,9,10,11,12,13,14,15,16,18,19,20,24
24	1,2,3,4,5,6,7,8,9,10,11,12,13,14,15,16,17,18,19,20,21,22,23,24

Table 14. Optimum features in feature selection groups

The optimal features in each subset were used for the MLC classification tests. The classification results were compared in *Figure 18*. The feature selection module demonstrated that, with twelve optimal features, the overall classification accuracy achieved 89.7% in correct and the average classification accuracy achieved 81.8% in correct. The overall accuracy was about 2% lower than the classification result from the full feature set and the average accuracy was about 4% lower than the result from the full feature set. However, the total number of the spectral bands required to achieve this level

of classification accuracies was only 12 features, which was 50% less than the full set of the twenty-four spectral bands. These twelve features included bands 1, 2, 4, and 7 from the 1985 image, Band 1, 2, and 7 from the 1990 image, bands 1, 3, and 7 from the 1996 image, and Band 1 and Band 7 from the 2001 image.

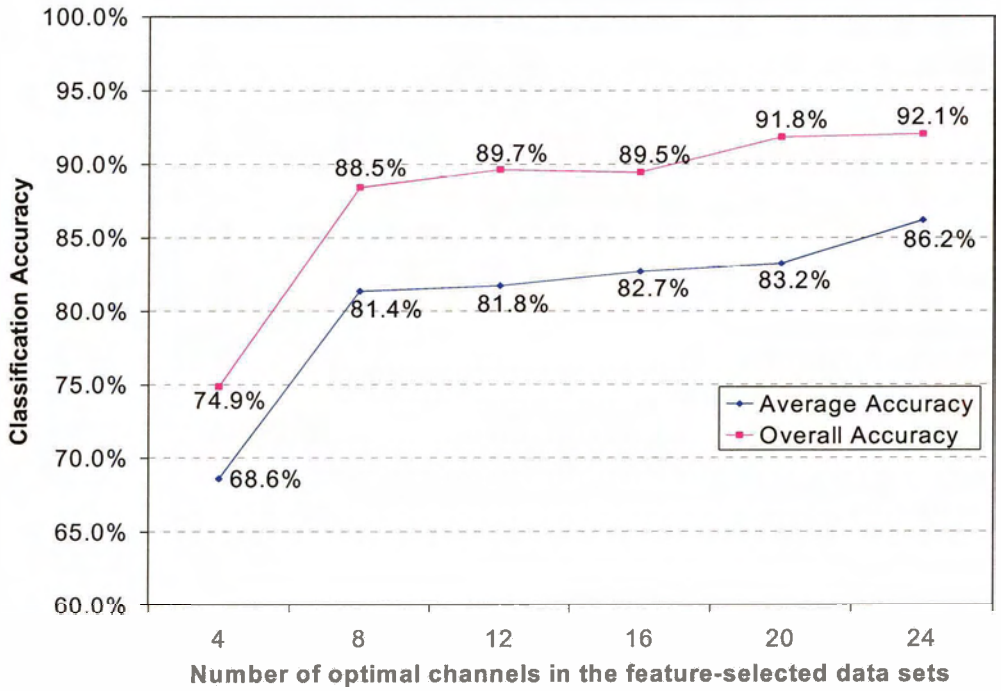

Figure 18. Classification with different optimal feature sets

If these twelve features were used for multitemporal classification, more dates of Landsat images could be added to the fused data set for analysis. If much more dates of Landsat images needed to be fused into the data set, four optimal features form Feature Selection could be used. In these results, the 1996 Landsat-5 TM image would have been

dropped from the fused Landsat data set and would not have participated in the image segmentation and classification process.

6.9 Landsat Image Classifications

Landsat classifications of the segments with all spectral bands were performed with the KPACS Euclidean, Maximum likelihood, and Adaptive Classifier. The KPACS Euclidean classification results were compared to the pixel-based Euclidean classification results computed from PCI Geomatica™ Imageworks®. The comparison results are shown in *Table 15*. The classification accuracies from the spatial-based Euclidean classifier in KPACS were about 10% higher than the accuracies from the pixel-based Euclidean classifier in PCI Geomatica™ Imageworks®. The confusion matrices for the KPACS and PCI Euclidean classifications are in Appendix B and Appendix C.

Landsat censor	Classification accuracy	Spatial-based Euclidean KPACS	Pixel-based Euclidean PCI Imageworks
1985 Landsat-5 TM	Average	81.4%	70.5%
1985 Landsat-5 TM	Overall	94.2%	82.4%
1990 Landsat-5 TM	Average	80.6%	72.1%
1990 Landsat-5 TM	Overall	95.4%	82.2%
1996 Landsat-5 TM	Average	79.7%	72.0%
1996 Landsat-5 TM	Overall	95.2%	83.2%
2001 Landsat-7 ETM+	Average	80.8%	73.7%
2001 Landsat-7 ETM+	Overall	86.0%	80.3%

Table 15. Spatial-based classification vs. pixel-based classification

To improve the multitemporal segment classifications, the KPACS Maximum Likelihood and Adaptive classifications were performed. The detailed classification

accuracies are shown in *Table 16*. The best classification results for the 1985, 1990, and 2001 classifications were produced with the Maximum Likelihood classifier, and the best classification accuracies for the 1996 Landsat image were generated by the Adaptive classifier. The confusion matrices for these classifications can be found in Appendix D.

	1985 Landsat-5	1990 Landsat-5	1996 Landsat-5	2001 Landsat-7
Class Label	Accuracy	Accuracy	Accuracy	Accuracy
Coniferous	99.0%	99.6%	99.5%	96.6%
Deciduous	95.1%	92.8%	96.0%	92.7%
Mixed wood	65.5%	74.1%	70.2%	71.9%
Clear-cut areas	99.0%	98.5%	99.5%	95.5%
Reforestation	81.4%	76.9%	58.4%	67.4%
Rocks	89.5%	96.7%	89.5%	95.5%
Clear Land	100.0%	100.0%	69.3%	100.0%
Scrub coniferous	64.8%	65.7%	97.6%	94.2%
Scrub deciduous	83.8%	87.6%	23.5%	69.9%
Mining areas	88.4%	84.2%	66.7%	97.5%
Water (dark)	89.7%	100.0%	100.0%	100.0%
Water (blue)	100.0%	100.0%	100.0%	100.0%
Clouds	100.0%	100.0%	100.0%	100.0%
Cloud shadow	100.0%	99.8%	98.0%	85.7%
Average accuracy	**89.7%**	**91.2%**	**84.4%**	**90.3%**
Overall accuracy	**97.3%**	**97.9%**	**96.7%**	**93.0%**

Table 16. Classification accuracies for each single date

Two of the low classification accuracies occurred between the Scrub coniferous and Scrub deciduous classes. Landsat TM and ETM+ were unable to discriminate scrub-coniferous from scrub-deciduous effectively. For an example, 71% of the Scrub deciduous in 1996 was misclassified as the Scrub coniferous (See the confusion matrix in Part (c) of Appendix D). To improve the classification accuracies on these classes, new sensors are required [7].

Figure 19 shows an example of the spatial-based classification image in Hinton, AB, generated from the 2001 Landsat-7 ETM+ image. As the creation of the training channel was only based on the set of the early-date forest inventory maps, detailed forest inventory plots and fieldwork are required to further validate the KPACS classification results.

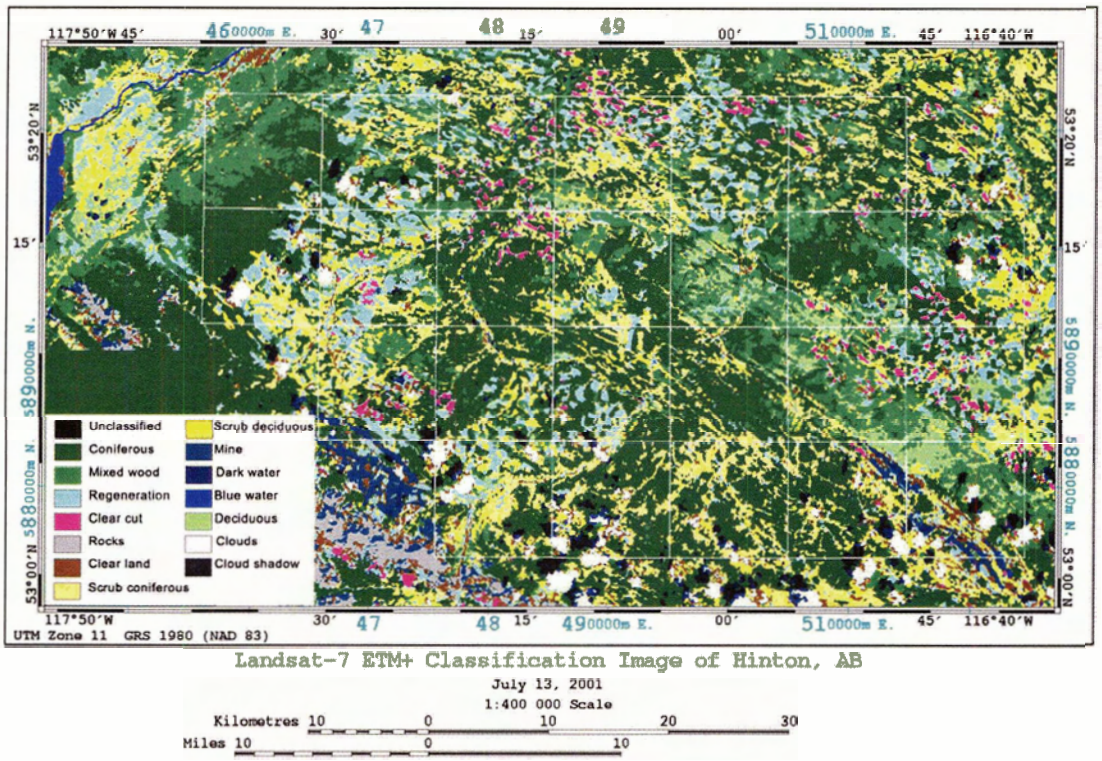

Figure 19. Classification image from 2001 Landsat-7 ETM+

6.10 Biomass and Aboveground Carbon

The Landsat vegetation biomass and aboveground carbon were computed from the forested areas in the 24 Township-Ranges of the Hinton study area. The forest stands

were classified as Coniferous, Deciduous, and Mixed wood. The Landsat carbon results were compared with the carbon numbers calculated from the Canadian Forest Inventory (CanFI) data.

A 2001 Landsat aboveground carbon distribution map created by the KPACS carbon module is illustrated in *Figure 20*. The largest amount of aboveground carbon occurs in the northwest and in a broad strip from the central area to the southeast of the study region. The non-forested areas in the carbon image are set to "0" (black areas). The white grid squares in the image represent the 24 township ranges of the Hinton study area. Each township range is 10 km by 10 km.

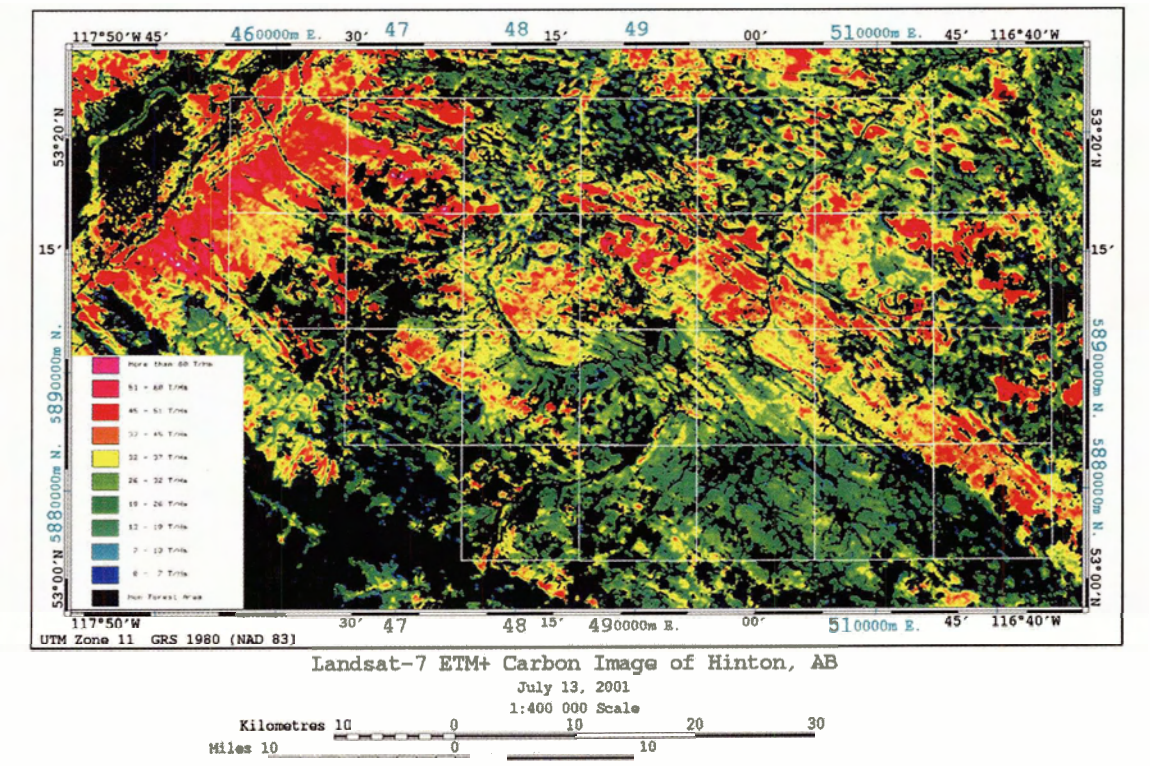

Figure 20. Aboveground carbon image for 2001 in Hinton, AB

The total aboveground carbon in megatonnes in the 24 township ranges of each date is shown in *Figure 21.*

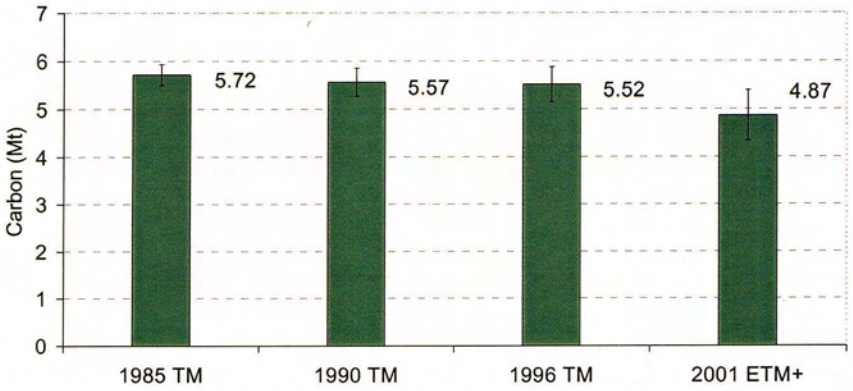

Figure 21. Total carbon in Hinton from multitemporal Landsat images

The range of the Landsat carbon relationship discussed in Section 4.7 is applicable to stand volume between 61 m^3/ha and 300 m^3/ha [37]. At greater stand volumes, canopy closure becomes closed and it is not possible for Landsat imagery to detect increased stand volumes. At low stand volumes, the spatial pattern of the scene components (tree shadow, crowns, and ground exposure) is much more variable, which decreases estimation accuracies by the KPACS carbon model. The stand volume ranges of the KPACS biomass are listed in *Table 17* and *Table 18. Table 17* gives the mean values of stand volume per pixel for the multitemporal Landsat data set. *Table 18* shows the number of pixels in each date that have biomass volume either less than 62 m^3/ha or higher than 300 m^3/ha. 99% of the biomass pixels have valid biomass values.

Landsat biomass/pixel	Mean (m^3/ha)	Standard deviation	Maximum (m^3/ha)
1985 Landsat biomass	155	40.1	288
1990 Landsat biomass	181	34.6	320
1996 Landsat biomass	161	36.9	304
2001 Landsat biomass	158	37.7	304

Table 17. Stand volume ranges and weighted accuracies

Landsat biomass	Total pixels	Pixels < 62 m^3/ha	Pixels >300 m^3/ha	% of out-range pixels
1985 Landsat biomass	2740981	28880	0	1.05%
1990 Landsat biomass	2669453	10763	485	0.42%
1996 Landsat biomass	2553082	21589	42	0.85%
2001 Landsat biomass	2294939	15999	23	0.70%

Table 18. Number of low and high stand-volume pixels

The accuracies of the multitemporal Landsat aboveground carbon were obtained by (14) and the results are listed in *Table 19*:

Biomass accuracy = (62 m^3/ha < Pixels < 300 m^3/ha) / Total number of pixels ×

Overall classification accuracy × Cloud deduction (14)

Landsat biomass	Accuracy
1985 Landsat biomass	96.2%
1990 Landsat biomass	94.8%
1996 Landsat biomass	93.4%
2001 Landsat biomass	89.2%

Table 19. Biomass accuracies

The total Landsat aboveground carbon in the twenty-four township ranges was also compared with the carbon estimates from the CanFI data (See *Table 20*). The CanFI data consisted of forest attributes tabulated on a 10 km by 10 km cell. The forest inventory summary statistics were provided by the Canadian provinces and territories based on their detailed forest inventory. The CanFI data were stored in an Oracle relational database. The attributes pertaining to the Hinton study site were extracted from the CanFI database. These attributes included Cell identifier, Stock, Maturity, Forest type, Biomass area, Biomass tonnes, and volumes. The CanFI carbon numbers for each township ranges were obtained by dividing the biomass by 2 [22]. The first acquisition of the CanFI attributes for the Hinton study area had a date of 1985. The second acquisition of the CanFI attributes had been updated to 2000.

	CanFI 85	CanFI 00	1985 TM	1990 TM	1996 TM	2001 ETM+	Average TM
Forest Area (Ha)	85906	95893	171598	167029	159893	143600	160530
Tonnes / Ha	68.3	59.0	33.3	33.3	34.5	33.9	33.8
Carbon (Mt)	5.87	5.66	5.72	5.57	5.52	4.87	5.42

Table 20. Carbon estimates from multitemporal Landsat images and CanFI data

The total carbon figures from both sources were in good agreement, with the average of the Landsat aboveground carbon estimates of 5.42 megatonnes. However, the average of the Landsat forested areas was about 1.67 times larger than the forested areas in the 2000 CanFI database. The average of the Landsat biomass was about 50% lower than the number from CanFI. The Landsat estimates showed the decreased forest areas and aboveground carbon, but the CanFI data indicated increased forested areas and decreased aboveground carbon over the period from 1985 to 2000.

With the 24 Township-Ranges available, further carbon comparison between Landsat and CanFI was examined on the individual Township-Ranges. *Figure 22* shows the comparison results. The correlation between the Landsat carbon and CanFI carbon at this level was not in good agreement. The CanFI data showed much more carbon than Landsat in some of Township-Ranges, but showed much less carbon than Landsat in the others.

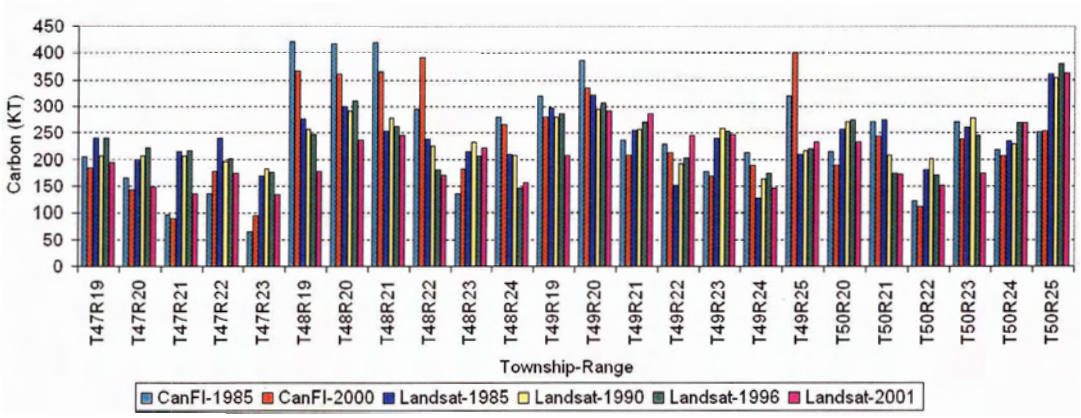

Figure 22. Carbon comparisons between CanFI and Landsat results

The advantage in using Landsat images to analyze forest cover and aboveground carbon was that the input data and final products were actually the images, which could be visualized and examined. Thus, by visualizing each Township-Range in the Landsat images, the differences between the Landsat carbon and CanFI carbon were investigated.

One of the examples was to look at the township-range T49R25, in which CanFI showed the most aboveground carbon, but Landsat showed much less. *Figure 23* illustrates a series of Landsat images revealing the forest cover changes in that area from

1985 to 2001. Forest clearcut activities have occurred since 1985. Less than 65% of the forests were left in T49R25.

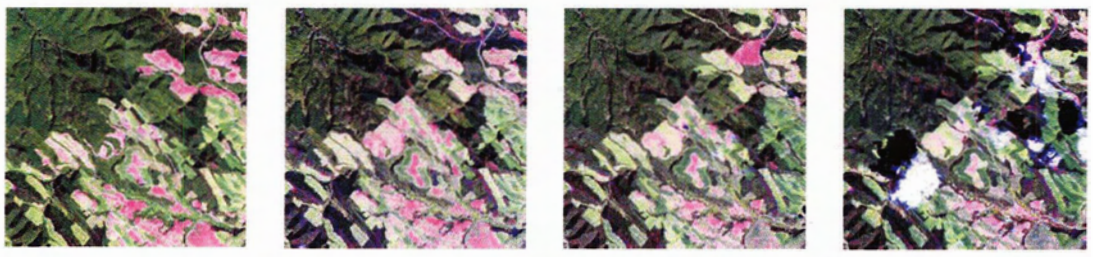

Figure 23. Forest covers in T49R25 visualized from Landsat images

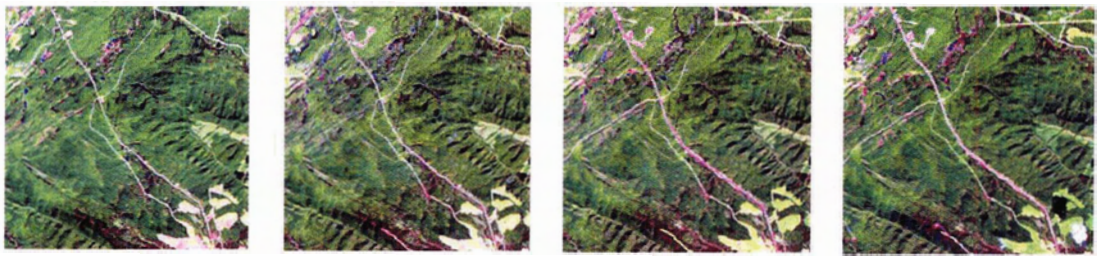

Figure 24. Forest covers in T50R25 visualized from Landsat images

Another example was to look at the township range T50R25. The carbon statistics from CanFI showed much less carbon than Landsat. From *Figure 24*, the multitemporal Landsat images showed that the most of forested areas in the area were mature forests and have not been disturbed since 1985.

Clearly, the biomass and aboveground carbon estimates based on the CanFI database had errors. The remote sensing procedures for image classification and carbon

estimation, on the other hand, provided consistent biomass and carbon results. Thus, by combining the remote sensing approach to existing methodologies for estimating vegetation biomass and aboveground carbon, the results would be much more consistent and accurate for supporting Canada's reporting commitments on the sustainability of the forest resources in Canada.

The current Landsat biomass relationship was derived from the Canal Flats study site in BC. To improve the accuracies of the remote sensing carbon analysis in the Hinton study site, different biomass relationships for different forested areas should be developed in the future. Because ND45 saturates at different amounts depending upon the forest type and age class, ground sample plots with accurate measurements from the Weldwood Corporation are required.

Another plan to improve the remote sensing carbon analysis is to acquire remote sensing multi-polarization radar data, such as Envisat ASAR [47] imagery. Backscatter characteristics of different forest types and changes can be examined with alternate polarization (HH, VV, HV, and VH) of Synthetic Aperture Radar (SAR) data. In particular, polarimetric SAR methods will be used to understand foliage biomass in the Hinton study areas and how it changes over time. For example, SAR biomass estimates will be compared with the multitemporal Landsat carbon and CanFI carbon estimates and also compared to forest inventory map (Hinton, Alberta) developed by the Northern Forestry Centre of the Canadian Forest Service [48].

6.11 Afforestation, Reforestation, and Deforestation Measurements

The remote sensing Afforestation, Reforestation, and Deforestation (ARD) were computed for the multitemporal classifications of the 1985, 1990, 1996 and 2001 Landsat images. The 1990 classification image was set to the reference image since the Kyoto Protocol requires the participating nations to report afforestation, reforestation, and deforestation that have occurred since 1990.

The fifteen classes in the classification images were converted into the four basic land types, Forest, Non-forest, Regeneration and Unclassified (See *Table 21*). Forest included the three forest categories: coniferous, deciduous and mixed-wood. Unclassified consisted of the unclassified pixels, no-data areas, clouds and cloud shadow. Regeneration referred to young trees. All other classes were set to the No-forest type. These basic-land-type classification images were then used as the input to the KPACS ARD module.

Class	Land Type
Coniferous	Forest
Mixed Wood	Forest
Deciduous	Forest
Regeneration	Regeneration
Clearcut 1985	Non-Forest
Clearcut 1990	Non-Forest
Clearcut 1996	Non-Forest
Clearcut 2001	Non-Forest
Rocks	Non-Forest
Clear Land	Non-Forest
Scrub	Non-Forest
Mine	Non-Forest
Water Dark	Non-Forest
Water Blue	Non-Forest
No Data	Unclassified

Table 21. Classes to basic land-type conversion table

Based on the remote-sensing ARD definitions in Section 4.8, the remote-sensing afforestation is that new forests in the later Landsat images are detected on the non-forested lands in the previous Landsat image. For an example, a non-forested area was detected in 1990, but it became regeneration in 1996 and forest in 2001. This area would be labelled as Afforestation in 1996.

ARD	1990	1996	2001
Afforestation 1996	Non-Forest	Forest	Forest
Afforestation 1996	Non-Forest	Forest	Regeneration
Afforestation 1996	Non-Forest	Regeneration	Forest
Afforestation 1996	Non-Forest	Regeneration	Regeneration
Afforestation 2001	Non-Forest	Non-Forest	Forest
Afforestation 2001	Non-Forest	Non-Forest	Regeneration
Reforestation 1996	Forest	Regeneration	Forest
Reforestation 1996	Forest	Regeneration	Regeneration
Reforestation 2001	Forest	Forest	Regeneration
Reforestation 2001	Forest	Non-Forest	Forest
Reforestation 2001	Forest	Non-Forest	Regeneration
Reforestation 2001	Regeneration	Non-Forest	Forest
Reforestation 2001	Regeneration	Non-Forest	Regeneration
Deforestation 1996	Forest	Non-Forest	Non-Forest
Deforestation 1996	Regeneration	Non-Forest	Non-Forest
Deforestation 2001	Forest	Forest	Non-Forest
Deforestation 2001	Forest	Regeneration	Non-Forest
Deforestation 2001	Regeneration	Forest	Non-Forest
Deforestation 2001	Regeneration	Regeneration	Non-Forest
Forest	Forest	Forest	Forest
Forest	Regeneration	Forest	Forest
Forest	Regeneration	Forest	Regeneration
Forest	Regeneration	Regeneration	Forest
Forest	Regeneration	Regeneration	Regeneration
Non-Forest	Non-Forest	Forest	Non-Forest
Non-Forest	Non-Forest	Non-Forest	Non-Forest
Non-Forest	Non-Forest	Regeneration	Non-Forest

Table 22. ARD permutations for the 1990, 1996, and 2001 Landsat images

The remote-sensing reforestation is that the planting of forests on lands that have been clear-cut areas in the earlier remote sensing images. For an example, a forested area was cut in 1990, but it became regenerated in 1996 and 2001. This area would be defined as Reforestation in 1996.

Moreover, the remote sensing deforestation is that forested lands in the early-date Landsat images are converted to the non-forested lands, on which there is no reforestation detected in the later Landsat images. For an example, a forested area was cut in 1990, but it became non-forested land in 1996 and 2001. This area would be identified as Deforestation in 1996. An ARD permutation table with the twenty-seven permutations was constructed in KPACS, shown in *Table 22*. Under IPCC rules, a thirty-year period is recommended if there is no evidence of land use change. The use of remote sensing to monitor deforestation will likely lead to changes in the IPCC rules.

By applying the KPACS ARD module to the four Landsat classification images, the remote-sensing afforestation, reforestation, and deforestation measurements in the Hinton study area were computed. During the ARD computation, an "Unclassified" area, such as cloud and shadow, in any of the basic-land-type classification images resulted in a "0" in the ARD images (6% of the twenty-four township ranges). *Figure 25* shows the spatial distribution of the ARD classes generated by the 1990, 1996 and 2001 Landsat classification images.

The ARD estimates were calculated from the ARD images. *Table 23* lists the detailed ARD statistics in year 1996 and 2001. The total afforestation and reforestation areas in the year 2001 were increased by around 2% of the twenty-four township ranges in the Hinton study area. The total deforestation in 2001 was about 3% of the twenty-four

township ranges higher than the 1996 level. The deforestation areas were roughly balanced with the total areas of afforestation and reforestation in each date.

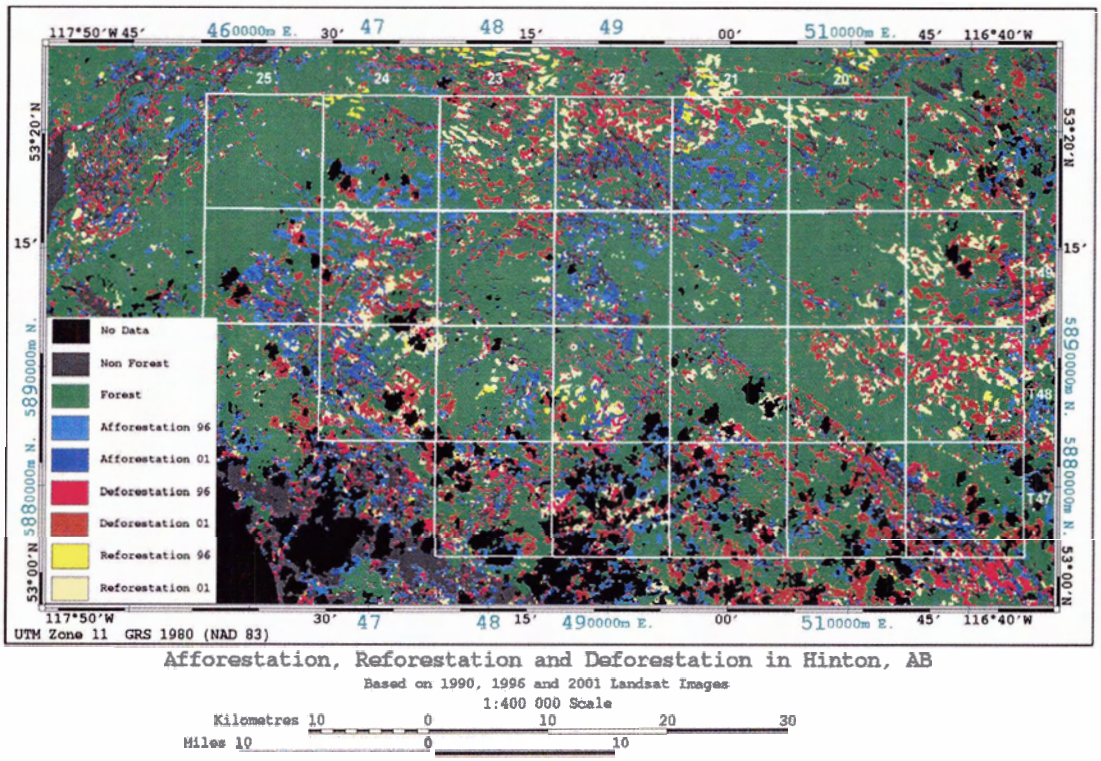

Figure 25. The Afforestation, Reforestation, and Deforestation map generated from the 1990, 1996 and 2001 Landsat classification images

Year	1996	2001
Afforestation (Ha)	5247 (2.3%)	9469 (4.2%)
Reforestation (Ha)	8571 (3.8%)	13762 (6.0%)
Deforestation (Ha)	13975 (6.1%)	20720 (9.1%)

Table 23. Afforestation, Reforestation, and Deforestation in 1996 and 2001

7 Conclusions and Future Research

7.1 Conclusions

A new computing system, KPACS, for processing multitemporal Landsat images and computing the Kyoto-Protocol products has been implemented in this thesis. The advanced features of KPACS include multitemporal Landsat image segmentation, feature selection, adaptive classification, aboveground carbon measurements, and Afforestation, Reforestation, and Deforestation (ARD) calculations.

Four dates of the Landsat images over the Hinton study area in Alberta, Canada were collected from 1985, 1990, 1996 and 2001 for evaluating KPACS. The images were geometrically corrected and radiometrically normalized. The segmentation process was performed on the fused multitemporal Landsat data set to create homogenous segment objects. These segments in each Landsat image were first classified with the KPACS Euclidean classifier, and the classification results showed 10% better than the classification results from the pixel-based Euclidean classifier in PCI.

To improve the classification accuracies, the KPACS Maximum Likelihood and Adaptive classifiers were applied to the multitemporal Landsat images. The best classification accuracies for the 1985, 1990, and 2001 Landsat images were obtained from the Maximum Likelihood Classifier. The best classification accuracies for the 1996 Landsat image were from the Adaptive classifier. The average classification accuracies over the 15 land-cover classes were between 84.4% and 91.2%. The overall classification accuracies were in the range between 93.0% and 97.9%.

The feature selection functionality was demonstrated with the twelve selected features in the 24-band multitemporal Landsat imagery. The overall classification accuracy achieved with these twelve features was 89.7% correct, which was only about 2% lower than the result from the full feature set, and the average classification accuracy was 81.8% correct, about 4% lower than the result from the full feature set. With only twelve spectral bands in use, more dates of Landsat images could have been added to the fused data set for analysis.

The Landsat aboveground carbon and ARD were measured in the forested areas specified in the classification images. Multitemporal carbon and ARD distribution maps were created. The Landsat aboveground carbon estimates were compared with the carbon numbers from the Canadian Forest Inventory (CanFI). The total carbon numbers agreed with each other. But, the Landsat forested areas were about 1.67 times larger than the CanFI forested areas; the average Landsat biomass was about 50% lower than the CanFI biomass. One reason was that the remote sensing analysis considered all forested areas; nevertheless, CanFI were focused on the commercial forest sites. Another reason could be that KPACS used a single Landsat biomass relationship to measure aboveground carbon in the entire study area.

The carbon comparison was also performed at the Township-Range level. Through the comparisons in the township-range T49R25 and T50R25, the remote sensing analysis was able to identify errors existing in the CanFI data.

The ARD products were computed through the change detection analysis and post classification comparisons. The total afforestation and reforestation areas in the study site

during the 1996-2001 period were almost doubled at the 1996 level, but they were roughly balanced with the total areas of deforestation in the same period.

The remote sensing approach for multitemporal classification, carbon analysis and ARD measurements in this thesis has shown that remote sensing provides an alternative and economic way to determine forest parameters over large areas and to validate aboveground carbon results from CanFI and CBM-CFS2. The remote sensing approach is a new addition to the current existing methodologies for supporting Canada's reporting commitments on the sustainability of its forest resources.

7.2 Future Research

There are several avenues for future research. The segment-based classification accuracies can be further improved with the new sensing technologies provided by the next generation of Landsat sensors. Such new technologies include more multispectral bands, high-resolution panchromatic channel, better data quantization and improved signal-to-noise ratios. The accuracies of the Landsat aboveground carbon analysis can also be improved by using different biomass relationships for different forested areas based on temporary and permanent sample plots from study areas. To support building multi-relationships, high spatial resolution (<1m GSD) imagery, such as Quickbird imagery, and multi-polarization Synthetic Aperture Radar (SAR) data, such as Envisat ASAR imagery, can be acquired and used to delineate individual tree crowns and examine backscatter characteristics of different forest types with alternate polarization respectively for detailed forest biomass. SAR data that interacts with branch and trunk

components, such as P-band SAR, can give direct measurements of biomass independent of forest species. It is recommended that further experiments using KPACS and the preceding improvements be conducted on data of other countries.

Bibliography

1. Natural Resources Canada, *1999-2000 Forests in the New Millennium*, in *The state of Canada's forests*. Pacific Forestry Centre, Natural Resources Canada, Victoria, BC, Canada 2000.
2. Government of Canada, *Canada and the Kyoto Protocol*. Government of Canada, 2003. http://www.climatechange.gc.ca/english/whats_new/overview_e.html
3. USGS, *Landsat Project Website*. U.S. Geological Survey, 2003. http://landsat7.usgs.gov/index.php
4. UN, *Kyoto Protocol to the United Nations Framework Convention on Climate Change*, in *Conference of the Parties*. United Nation: Kyoto, Japan 1997. http://www.cop4.org/resource/docs/cop3/l07a01.pdf
5. Kurz, W.A., M. Apps, E. Banfield, and G. Stinson, *Forest carbon accounting at the operational scale*. The Forestry Chronicle, vol. 78, pp. 5, 2002.
6. Goodenough, D.G., A. Dyk, K.O. Niemann, J. Pearlman, A.S. Bhogal, H. Chen, T. Han, M. Murdoch, and C. West, *Processing Hyperion and ALI for Forest Classification*. IEEE Transactions on Geoscience and Remote Sensing, vol. 41, issue 6, pp. 1321-1331, 2003.
7. Chen, H., D.G. Goodenough, A. Dyk, S. McDonald, and T. Han. *Change Detection with ALI and Landsat satellite data*. in Proc. *Second International Workshop on the Analysis of Multitemporal Remote Sensing Images*. Ispra (VA), Italy, 2003.
8. Goodenough, D.G., A.S. Bhogal, H. Chen, and A. Dyk. *Comparison of Methods for Estimation of Kyoto Protocol Products of Forests from Multitemporal Landsat*. in Proc. *IGARSS 2001*, vol. 2, pp. 764-767, Sydney, Australia, 2001.
9. Goodenough, D.G., B. Guindon, N.A. Swanberg, and J.F. Meunier. *SAR Experiment with Adaptive Filtering to Improve Image Segmentation*. in *ISPRS Working Group on SAR*. Tokyo, Japan, 1983.
10. Goodenough, D.G., *TM and SPOT Integration with GIS*. Phot. Eng. & Rem. Sens., Vol. 54, pp. 167-176, 1988.
11. Sheffner, E., *Coverage history of Landsat satellites*. The Ecosystem Science and Technology Branch of the Earth Science Division at Ames Research Center, 1999. http://geo.arc.nasa.gov/sge/landsat/landsat.html
12. Department of Geography, University of Wales Swansea, *Landsat 5 Thematic Mapper Images of Swansea Bay and Environs*, Department of Geography, University of Wales Swansea. http://ralph.swan.ac.uk/level_1/landband.htm
13. Earth Observation Centre, *Landsat*. Earth Observation Centre, National Space Development Agency of Japan, 2002. http://www.eoc.jaxa.jp/satellite/satdata/landsat_e.html
14. Lillesand, T.M. and R.W. Kiefer, *Remote Sensing and Image Interpretation*. Second Edition ed. John Wiley & Sons Inc., 1987.
15. Hall, R., *Alberta - Foothills Model Forest*. Natural Resources Canada, 2003. http://www.cfl.cfs.nrcan.gc.ca/ECOLEAP/pilot_regions/alberta_e.html
16. Price, D.T., R. Hall, F. Raulier, M. Lindner, B. Case, and P. Bernier, *Simulating Climatic Impacts on, and Adaptive Mamagement Options for, Boreal Forest Ecosystems in Western Canada*. Canadian Forest Service (CFS), Northern Forestry Centre: Edmonton, AB, Canada, 2002.
17. PCI Geomatics, *Geomatica 9 Software Solutions*. PCI Geomatics: Ontario Canada, 2003. http://www.pcigeomatics.com/
18. ENVI, *ENVI? The Future of Remote Sensing*. 2003, Research System Inc., 2003. http://www.rsinc.com/envi/index.cfm

19. eCognition, *eCognition Objected Oriented Image Analysis 3.0.* Definiens Imaging, 2003. http://www.definiens-imaging.com/product.htm
20. Jackson, Q. and D. Landgrebe. *Adaptive Bayesian Contextual Classification Based on Markov Random Fields.* in Proc. *IGARSS 2002*, vol. 3, pp. 1422-1424, Toronto, Canada, 2002.
21. Jiang, M., *Markov Random Fields and Application.* Department of Information Science, School of Mathematics, Peking University, 2001. http://ct.radiology.uiowa.edu/~jiangm/courses/mm-cv-ip/node38.html
22. Jackson, Q. and D. Landgrebe, *Design Of An Adaptive Classification Procedure For The Analysis Of High-Dimensional Data With Limited Training Samples*, in *School of Electrical & Computer Engineering.* Purdue University: West Lafayette, 2001.
23. Jia, X., *Cluster-space Representation for Hyperspectral Data Classification.* IEEE Transactions on Geoscience and Remote Sensing, vol. 40, pp. 593-598, 2002.
24. Kurz, W.A. and M.J. Apps, *A 70-Year Retrospective Analysis of Carbon Fluxes in the Canadian Forest Sector.* Ecological Applications, Vol. 9(2), pp. 526-547, 1999.
25. Meunier, J.F., K. Staenz, H. DesRosiers, and Q. Bradley, *LDIAS Software Description - SEGGRA.* Advanced Forest Technologies, Pacific Forestry Centre, Victoria, BC, Canada, 1982.
26. Eastman, J.R., *Idrisi 32 Release 2*, in *Guide to GIS and Image Processing.* Worcester. pp. 17-34, 2001.
27. PCI, *Using PCI Software.* 1996, PCI Geomatics: Ontario Canada. http://www.pcigeomatics.com/
28. Tou, J.T. and R.C. Gonzalez, *Pattern Classification by Distance Functions*, in *Pattern Recognition Principles.* 1974, Addison-Wesley Publishing Company: London.
29. Dyk, A., *MAKETRU.* 1999, Advanced Forest Technologies, Pacific Forestry Centre: Victoria, BC.
30. Teillet, P.M., K. Staenz, C. Phillip, A.M. Cardill, W.E. Reiche, J.F.M. Handle, D. Schanzer, and Q. Bradley, *LDIAS Software Description - GSTAT.* Advanced Forest Technologies, Pacific Forestry Centre: Victoria, BC, 1983.
31. Goodenough, D.G., P.M. Narendra, and K. O'Neill, *Feature Subset Selection in Remote Sensing.* Cnd. J. Rem. Sens., 1978. Vol.4(No.2): pp. 143-148.
32. Narendra, P.M. and K. Fukunaga, *A Branch and Bound Algorithm for Feature Subset Selection.* 1977 IEEE Transaction on Computers, 1977(C-26): pp. 917-921.
33. Meunier, J.F., A. Menard, and J.T. Folinsbee, *LDIAS Software Description - FEATUR.* Advanced Forest Technologies, Pacific Forestry Centre: Victoria, BC, 1981.
34. Tou, J.T. and R.C. Gonzalez, *Pattern Classification by Likekihood Functions*, in *Pattern Recognition Principles.* 1974, Addison-Wesley Publishing Company: London.
35. Jackson, Q. and D. Landgrebe, *An Adaptive Classifier Design for High-Dimensional Data Analysis with a Limited Training Data Set.* IEEE Transactions on Geoscience and Remote Sensing, Vol. 39(No. 12): p. 2664-2679, 2001.
36. Goodenough, D.G., A.S.P. Bhogal, A. Dyk, M. Apps, R. Hall, P. Tickle, H. Chen, K. Butler, and M. Gim. *Determination of Above-Ground Carbon in Canada's Forests - A Multi-Source Approach.* In Proc. *IGARSS 2000.* vol. 3, pp. 949-953, Honolulu, Hawaii, 2000.
37. Gemmell, F.M. and D.G. Goodenough. *Estimating Timber Volume from TM Data: The Importance of Scale and Accuracy of Forest Cover Data.* in *18th Annual Conference of Remote Sensing Society.* 1992. University of Dundee, Scotland.
38. Price, D.R., D.H. Halliwell, M.J. Apps, W.A. Kurz, and S.R. Curry, *Comprehensive assessment of carbon stocks and fluxes in a Boreal-Cordilleran forest management unit.* Can. J. For. Res., Vol. 27, pp. 2005-2016, 1998.

39. Neilson, R.W., J. Dobie, and D.M. Wright, *Conversion Factors for Forest Products Industry in Western Canada.* Forintek Canada Corp., Vancouver, BC, Special Publication SP-24R, 1985.
40. Dyk, A., *CARBON.* Advanced Forest Technologies, Pacific Forestry Centre: Victoria, BC, 1999.
41. Watson, R.T., I.R. Noble, B. Bolin, N.H. Ravindranath, D.J. Verardo, and D.J. Dokken, *Land Use, Land-Use Change and Forestry.* Bonn Germany: The Intergovernmental Panel on Climate Change (IPCC), 1998. http://www.grida.no/climate/ipcc/land_use/038.htm
42. Dyk, A. and Q. Bradley, *RIASSA.* Advanced Forest Technology, Pacific Forestry Centre: Victoria, BC, 2001.
43. Hughes, G.F., *On the Mean Accuracy of Statistical Pattern Recognition.* IEEE Transactions Information Theory, Vol. IT-14(No. 1), pp. 55-63, 1968.
44. Landgrebe, D., *Information Extraction Principles and Methods for Multispectral and Hyperspectral Image Data*, in *Information Processing for Remote Sensing*, C.H. Chen, Editor. The World Scientific Publishing Co., Inc.: River Edge, 2000.
45. Dyk, A., D.G. Goodenough, A.S. Bhogal, J. Pearlman, and J. Love. *Geometric Correction and Validation of Hyperion and ALI Data for EVEOSD.* In Proc. *IGARSS 2002*, vol. 1, 579-583, Toronto, ON, Canada, 2002.
46. Resource Evaluation and Planning Division for the Alberta Forest Service, *Hinton Forest Inventory Map.* 1:40000, Resource Evaluation and Planning Division for the Alberta Forest Service: Alberta, 1993.
47. European Space Agency, *ESA Envisat Instruments - ASAR.* European Space Agency, 2003. http://envisat.esa.int/instruments/asar/
48. Hall, R.J., B.S. Case, E. Arsenault, D.T. Price, J.E. Luther, D.E. Piercey, L. Guindon, and R.A. Fournier. *Modelling and Mapping Forest Biomass using Forest Inventory and Landsat TM Data: Results from the Foothills Model Forest, Alberta.* in Proc. *2002 IEEE International Geoscience and Remote Sensing Symposium and the 24th Canadian Symposium on Remote Sensing*, vol. 3, pp. 1320-1323, Toronto, Canada, 2002.

Appendix A. Implementation of Branch and Bound Algorithm

Simplified pseudo code of the Branch and Bound algorithm:

```
Current_Node = The Top Node in the Tree
Current_Bound = 0
Current_Level = 0

LIST(Current_Level): Containing all nodes at Level = Current_Level + 1 directly
connected to the the Current_Node.

Evaluate_Criterion ( ) {
    IF LIST(Current_Level) = { } THEN
        Current_Level = Current_Level - 1
        IF Current_Level = -1 THEN
            STOP  (Search is completed.)
        ELSE
            Evaluate_Criterion ( )
        ENDIF
    ELSE
    Compute the Divergence Criterion, J, for the first Node in LIST(Current_Level).
        IF J > Current_Bound THEN
            IF Current_Level = M -1 (First node in List at level M) THEN
                Current_Bound = J
                Best_Node = First node in LIST(Current_Level)
                Remove first Node from LIST(Current_Level)
                Evaluate_Criterion ( )
            ELSE
                Current_Node = First node in LIST(Current_Level)
                Remove first Node from LIST(Current_Level)
                Current_Level = Current_Level + 1
                Update LIST(Current_Level)
                Evaluate_Criterion ( )
            ENDIF
        ELSE
            Remove First Element from LIST(Current_Level)
            Evaluate_Criterion ( )
        ENDIF
    ENDIF
```

Appendix B. Confusion Matrix of Spatial-based Euclidean Classification

a) Confusion matrix of the spatial-based Euclidean classification for 1985 Landsat-5 TM

Areas		Percent Pixels Classified by Code													
Class	Pixels	1	5	6	7	13	16	18	19	26	30	31	32	33	34
1: Conifers	180581	96.2	3.8	0.0	0.0	0.0	0.0	0.0	0.0	0.0	0.0	0.0	0.0	0.0	0.0
5: Mixed Wood	3309	7.4	78.6	0.0	0.0	0.0	0.0	0.0	0.0	0.0	0.0	0.0	0.0	0.0	14.0
6: Regeneration	3748	0.0	0.0	86.2	0.0	0.0	0.0	0.0	11.4	0.0	0.0	0.0	0.0	0.0	2.4
7: Clear-cut 1985	8140	0.0	0.0	2.1	89.4	0.0	8.5	0.0	0.0	0.0	0.0	0.0	0.0	0.0	0.0
13: Rock	760	0.0	0.0	0.0	0.0	80.3	3.0	0.0	0.0	16.7	0.0	0.0	0.0	0.0	0.0
16: Clear Land	163	0.0	0.0	0.0	16.6	10.4	73.0	0.0	0.0	0.0	0.0	0.0	0.0	0.0	0.0
18: Scrub Coniferous	3040	0.0	10.2	2.6	0.0	0.0	0.0	66.1	21.1	0.0	0.0	0.0	0.0	0.0	0.0
19: Scrub Deciduous	1392	0.0	0.0	6.3	0.0	0.0	0.0	58.3	35.4	0.0	0.0	0.0	0.0	0.0	0.0
26: Mine	1150	15.6	0.0	0.0	1.8	0.2	13.7	4.4	0.0	64.3	0.0	0.0	0.0	0.0	0.0
30: Water Lake	2453	0.0	0.0	0.0	0.0	0.0	0.0	0.0	0.0	0.0	100	0.0	0.0	0.0	0.0
31: Water River	609	0.0	0.0	0.0	0.0	0.0	0.0	0.0	0.0	0.0	0.0	100	0.0	0.0	0.0
32: Cloud	1449	0.0	0.0	0.0	0.0	11.4	0.0	0.0	0.0	0.0	0.0	0.0	82.0	0.0	0.0
33: Cloud Shadow	3031	0.0	0.0	0.0	0.0	0.0	0.0	0.0	0.0	0.0	0.0	0.0	0.0	100	0.0
34: Deciduous	6203	0.0	6.5	0.0	0.0	0.0	0.0	0.0	5.1	0.0	0.0	0.0	0.0	0.0	88.4

Average accuracy = 81.42% Overall accuracy = 94.22% Kappa Coefficient = 0.82082

b) Confusion matrix of the spatial-based Euclidean classification for 1990 Landsat-5 TM

Areas		Percent Pixels Classified by Code														
Class	Pixels	1	5	6	7	8	13	16	18	19	26	30	31	34	37	38
1: Conifers	179309	98.2	1.7	0.0	0.0	0.0	0.0	0.0	0.0	0.0	0.0	0.0	0.0	0.0	0.0	0.0
5: Mixed Wood	3193	4.6	84.0	0.0	0.0	0.0	0.0	0.0	0.9	0.0	0.0	0.0	0.0	10.6	0.0	0.0
6: Regeneration	3276	0.0	0.0	83.2	0.0	0.0	0.0	0.0	0.0	0.0	0.0	0.0	0.0	16.8	0.0	0.0
7: Regeneration	8070	0.0	0.0	12.6	74.3	11.5	0.0	0.1	1.5	0.0	0.0	0.0	0.0	0.0	0.0	0.0
8: Clear-cut 1990	6382	0.0	0.0	0.0	0.0	98.9	0.0	0.0	1.1	0.0	0.0	0.0	0.0	0.0	0.0	0.0
13: Rock	760	0.0	0.0	0.0	0.0	0.0	80.3	9.2	0.0	0.0	10.5	0.0	0.0	0.0	0.0	0.0
16: Clear Land	163	0.0	0.0	0.0	0.0	0.0	10.4	89.6	0.0	0.0	0.0	0.0	0.0	0.0	0.0	0.0
18: Scrub Coniferous	2243	0.0	22.4	0.9	0.0	0.0	0.0	0.0	53.5	23.2	0.0	0.0	0.0	0.0	0.0	0.0
19: Scrub Deciduous	1335	0.0	0.0	11.2	0.0	0.0	0.0	0.0	60.8	28.0	0.0	0.0	0.0	0.0	0.0	0.0
26: Mine	1121	8.5	0.0	0.0	7.4	0.0	7.1	20.3	0.0	0.0	50.7	6.0	0.0	0.0	0.0	0.0
30: Water Lake	2453	0.0	0.0	0.0	0.0	0.0	0.0	0.0	0.0	0.0	0.0	82.8	0.0	0.0	0.0	17.2
31: Water River	609	0.0	0.0	0.0	0.0	0.0	0.0	0.0	0.0	0.0	0.0	0.0	100	0.0	0.0	0.0
34: Deciduous	6203	0.0	3.5	3.3	0.0	0.0	0.0	0.0	0.0	3.6	0.0	0.0	0.0	89.6	0.0	0.0
37: Cloud	4912	0.0	0.0	0.0	0.0	0.0	0.0	0.0	0.0	0.0	0.0	0.0	0.0	0.0	95.6	0.0
38: Cloud Shadow	7110	0.0	0.0	0.0	0.0	0.0	0.2	0.0	0.0	0.0	0.0	0.0	0.0	0.0	0.0	99.8

Average accuracy = 80.55% Overall accuracy = 95.41% Kappa Coefficient = 0.87987

c) Confusion matrix of the spatial-based Euclidean classification for 1996 Landsat-5 TM

Areas		Percent Pixels Classified by Code														
Class	Pixels	1	5	6	8	10	13	16	18	19	26	30	31	34	35	36
1: Conifers	179477	99.2	0.7	0.0	0.0	0.0	0.0	0.0	0.0	0.0	0.0	0.0	0.0	0.0	0.0	0.0
5: Mixed Wood	3309	12.6	68.0	0.4	0.0	0.0	0.0	0.0	1.8	2.2	0.0	0.0	0.0	15.1	0.0	0.0
6: Regeneration	6774	0.0	0.0	74.3	14.6	0.0	0.0	0.0	0.0	0.2	0.0	0.0	0.0	10.9	0.0	0.0
8: Regeneration	6382	0.0	0.0	9.0	89.5	0.4	0.0	0.0	1.1	0.0	0.0	0.0	0.0	0.0	0.0	0.0
10: Clear-cut 1996	9280	0.0	0.0	0.0	21.0	78.6	0.0	0.3	0.0	0.0	0.0	0.0	0.0	0.0	0.0	0.0
13: Rock	760	0.0	0.0	0.0	0.0	0.0	80.3	6.2	0.0	0.0	10.5	0.0	0.0	0.0	0.0	0.0
16: Clear Land	163	0.0	0.0	0.0	0.0	0.0	10.4	89.6	0.0	0.0	0.0	0.0	0.0	0.0	0.0	0.0
18: Scrub Coniferous	3040	0.0	8.5	0.0	0.0	0.0	0.0	0.0	43.3	48.3	0.0	0.0	0.0	0.0	0.0	0.0
19: Scrub Deciduous	1392	0.0	0.0	7.9	0.0	0.0	0.0	0.0	58.3	33.8	0.0	0.0	0.0	0.0	0.0	0.0
26: Mine	1150	8.7	0.0	3.2	22.6	0.0	0.0	4.3	0.0	0.0	50.5	10.6	0.0	0.0	0.0	0.0
30: Water Lake	2453	0.0	0.0	0.0	0.0	0.0	0.0	0.0	0.0	0.0	0.0	100	0.0	0.0	0.0	0.0
31: Water River	609	0.0	0.0	0.0	0.0	0.0	0.0	0.0	0.0	0.0	0.0	0.0	100	0.0	0.0	0.0
34: Deciduous	6203	0.0	2.9	0.4	0.0	0.0	0.0	0.0	0.8	5.8	0.0	0.0	0.0	90.0	0.0	0.0
35: Cloud	2449	0.0	0.0	0.0	0.0	0.0	2.3	0.0	0.0	0.0	0.0	0.0	0.0	0.0	95.2	0.0
36: Cloud Shadow	3253	0.0	0.0	0.0	0.0	0.0	0.0	0.0	0.0	0.0	0.0	0.0	0.0	0.0	0.0	100

Average accuracy = 79.69% Overall accuracy = 95.16% Kappa Coefficient = 0.86959

d) Confusion matrix of the spatial-based Euclidean classification for 2001 Landsat-7 ETM+

Areas		Percent Pixels Classified by Code													
Class	Pixels	1	5	6	11	13	16	18	19	26	30	31	34	39	40
1: Conifers	146387	87.9	10.2	0.0	0.0	0.0	0.0	1.7	0.0	0.0	0.1	0.0	0.0	0.0	0.1
5: Mixed Wood	2257	4.6	74.3	0.0	0.0	0.0	0.0	5.3	0.0	0.0	0.0	0.0	15.8	0.0	0.0
6: Regeneration	19489	0.4	3.6	74.5	0.0	0.0	0.2	1.5	6.6	0.1	0.2	0.0	12.8	0.0	0.0
11: Clear-cut 2001	8408	0.0	0.0	0.2	91.2	0.0	6.4	0.6	0.2	1.3	0.0	0.0	0.0	0.0	0.0
13: Rock	760	0.0	0.0	0.0	0.0	80.3	16.4	0.0	0.0	3.3	0.0	0.0	0.0	0.0	0.0
16: Clear Land	163	0.0	0.0	0.0	0.0	0.0	100	0.0	0.0	0.0	0.0	0.0	0.0	0.0	0.0
18: Scrub Coniferous	2949	0.1	2.6	3.8	0.0	0.0	0.1	64.4	28.9	0.0	0.0	0.0	0.0	0.0	0.0
19: Scrub Deciduous	1105	0.3	0.0	11.0	0.0	0.0	0.0	35.2	53.5	0.0	0.0	0.0	0.0	0.0	0.0
26: Mine	1001	9.4	0.0	1.5	0.0	0.8	33.3	17.4	0.0	37.0	0.7	0.0	0.0	0.0	0.0
30: Water Lake	2453	0.0	0.0	0.0	0.0	0.0	0.0	0.0	0.0	0.0	100	0.0	0.0	0.0	0.0
31: Water River	609	0.0	0.0	0.0	0.0	0.0	0.0	0.0	0.0	0.0	0.0	100	0.0	0.0	0.0
34: Deciduous	6203	0.0	3.8	2.6	0.0	0.0	0.3	0.5	3.9	0.0	0.0	0.0	88.8	0.0	0.0
39: Cloud	2712	0.0	0.0	0.0	0.0	4.4	0.1	0.0	0.0	0.0	0.0	0.0	0.0	93.4	0.0
40: Cloud Shadow	2502	0.5	0.0	0.0	0.0	0.0	0.0	0.4	0.0	0.0	13.8	0.0	0.0	0.0	85.3

Average accuracy = 80.76% Overall accuracy = 86.02% Kappa Coefficient = 0.72084

Appendix C. Confusion Matrix of Pixel-based Euclidean Classification

a) Confusion matrix of the pixel-based Euclidean classification for 1985 Landsat-5 TM

Areas		Percent Pixels Classified by Code													
Class	Pixels	1	5	6	7	13	16	18	19	26	30	31	32	33	34
1: Conifers	180581	84.6	9.9	0.3	0.1	0.0	0.0	1.8	0.4	0.1	0.0	0.0	0.0	2.6	0.3
5: Mixed Wood	3309	18.3	56.9	0.9	0.0	0.0	0.4	3.3	2.7	0.1	0.0	0.0	0.0	0.1	17.4
6: Regeneration	3748	0.0	0.2	81.2	1.2	0.1	0.4	1.5	12.1	0.1	0.0	0.0	0.0	0.0	3.2
7: Clear-cut 1985	8140	0.0	0.0	5.6	76.9	0.8	12.4	1.1	0.2	2.9	0.0	0.0	0.0	0.0	0.0
13: Rock	760	0.8	0.0	0.0	0.0	74.6	6.3	0.0	0.0	17.6	0.0	0.0	0.7	0.0	0.0
16: Clear Land	163	0.0	0.0	1.8	21.5	22.9	53.4	0.0	0.0	1.2	0.0	0.0	0.0	0.0	0.0
18: Scrub Coniferous	3040	4.9	17.7	5.7	0.1	0.0	0.0	37.7	32.3	0.0	0.0	0.0	0.0	0.0	1.5
19: Scrub Deciduous	1392	1.3	14.1	12.2	0.0	0.0	0.0	31.9	36.1	0.0	0.0	0.0	0.0	0.0	4.5
26: Mine	1150	12.6	0.1	0.0	7.3	1.7	18.6	3.0	0.0	56.7	0.0	0.0	0.0	0.0	0.0
30: Water Lake	2453	7.9	0.5	0.0	0.0	0.0	0.0	0.2	0.1	0.0	86.3	0.0	0.0	5.0	0.0
31: Water River	609	1.3	1.0	0.0	0.0	0.0	0.0	1.0	0.0	1.0	2.5	93.3	0.0	0.0	0.0
32: Cloud	1449	0.0	0.0	0.0	0.0	12.1	3.0	0.0	0.0	0.1	0.0	0.0	84.8	0.0	0.0
33: Cloud Shadow	3031	4.5	0.4	0.0	0.0	0.1	0.1	0.5	0.0	0.8	0.5	0.0	0.0	93.1	0.0
34: Deciduous	6203	0.7	17.6	2.4	0.0	0.0	0.0	1.9	6.4	0.0	0.0	0.0	0.0	0.0	71.0

Average accuracy = 70.5 Overall accuracy = 82.4 Kappa Coefficient = 0.81501

b) Confusion matrix of the pixel-based Euclidean classification for 1990 Landsat-5 TM

Areas		Percent Pixels Classified by Code														
Class	Pixels	1	5	6	7	8	13	16	18	19	26	30	31	34	37	38
1: Conifers	179309	83.9	10.8	0.1	0.1	0.0	0.0	0.1	1.4	0.3	0.2	0.0	0.0	0.3	0.0	2.7
5: Mixed Wood	3193	17.8	62.9	0.0	0.0	0.0	0.0	0.0	3.1	2.4	0.0	0.0	0.0	13.7	0.0	0.0
6: Regeneration	3276	0.0	0.5	70.2	8.9	0.0	0.0	0.1	0.7	2.9	0.1	0.0	0.0	16.8	0.0	0.0
7: Regeneration	8070	0.1	0.2	15.2	63.8	13.9	0.2	1.8	3.7	0.8	0.1	0.0	0.0	0.1	0.0	0.0
8: Clear-cut 1990	6382	0.2	0.2	0.1	4.8	88.9	0.6	2.4	1.3	0.1	1.4	0.0	0.0	0.0	0.0	0.0
13: Rock	760	0.0	0.0	0.0	0.0	0.0	80.5	10.9	0.0	0.0	8.6	0.0	0.0	0.0	0.0	0.0
16: Clear Land	163	0.0	0.0	1.2	14.7	8.6	8.6	61.4	0.0	0.0	5.5	0.0	0.0	0.0	0.0	0.0
18: Scrub Coniferous	2243	0.0	13.1	4.7	1.3	0.1	0.0	0.0	51.9	22.9	0.3	0.0	0.0	5.8	0.0	0.0
19: Scrub Deciduous	1335	0.0	13.4	14.5	0.0	0.0	0.0	0.0	35.2	35.0	0.0	0.0	0.0	1.9	0.0	0.0
26: Mine	1121	13.5	0.1	0.5	3.5	0.4	11.9	17.2	2.3	0.2	44.3	6.2	0.0	0.0	0.0	0.0
30: Water Lake	2453	6.6	0.4	0.0	0.0	0.0	0.0	0.0	0.2	0.1	0.1	83.7	0.0	0.0	0.0	8.9
31: Water River	609	1.5	0.0	0.0	0.0	0.0	0.0	0.0	0.0	0.0	3.0	1.2	94.4	0.0	0.0	0.0
34: Deciduous	6203	0.0	12.1	8.5	0.4	0.0	0.0	0.0	2.2	5.5	0.0	0.0	0.0	70.9	0.0	0.0
37: Cloud	4912	5.0	0.0	0.0	0.0	0.0	2.4	0.0	0.0	0.0	0.0	0.0	0.0	0.0	97.6	0.0
38: Cloud Shadow	7110	0.0	0.5	0.0	0.1	0.0	0.3	0.4	0.2	0.0	1.3	0.5	0.0	0.0	0.0	91.9

Average accuracy = 72.1 Overall accuracy = 82.2 Kappa Coefficient = 0.81575

c) Confusion matrix of the pixel-based Euclidean classification for 1996 Landsat-5 TM

Areas		Percent Pixels Classified by Code														
Class	Pixels	1	5	6	8	10	13	16	18	19	26	30	31	34	35	36
1: Conifers	179477	85.5	10.2	0.3	0.2	0.0	0.0	0.1	1.7	0.6	0.3	0.1	0.0	0.4	0.0	1.0
5: Mixed Wood	3309	23.3	53.3	1.7	0.4	0.1	0.0	0.1	3.5	1.6	0.1	0.0	0.0	15.9	0.0	0.0
6: Regeneration	6774	0.0	0.0	71.7	13.1	0.0	0.0	0.0	0.4	5.7	0.1	0.0	0.0	9.0	0.0	0.0
8: Regeneration	6382	0.2	0.1	5.9	79.6	9.5	0.0	1.6	1.4	1.2	0.6	0.0	0.0	0.0	0.0	0.0
10: Clear-cut 1996	9280	0.0	0.0	0.8	13.6	81.4	1.2	1.4	0.1	0.1	1.4	0.0	0.0	0.0	0.0	0.0
13: Rock	760	0.0	0.0	0.0	0.3	0.3	78.3	12.6	0.0	0.0	8.6	0.0	0.0	0.0	0.0	0.0
16: Clear Land	163	0.0	0.0	2.5	16.6	3.1	16.6	55.2	0.0	0.0	6.1	0.0	0.0	0.0	0.0	0.0
18: Scrub Coniferous	3040	3.7	18.4	2.4	0.3	0.0	0.0	0.0	36.5	37.2	0.1	0.0	0.0	1.4	0.0	0.0
19: Scrub Deciduous	1392	1.2	11.8	12.6	0.0	0.0	0.0	0.4	31.0	40.6	0.1	0.1	0.0	2.2	0.0	0.0
26: Mine	1150	6.1	0.0	7.3	12.6	0.1	1.6	6.5	0.5	1.0	51.9	12.4	0.0	0.0	0.1	0.0
30: Water Lake	2453	8.0	0.4	0.0	0.0	0.0	0.0	0.0	0.2	0.0	0.2	85.5	0.0	0.0	0.0	5.7
31: Water River	609	2.3	0.1	0.0	0.0	0.0	0.0	0.0	0.2	0.0	4.6	0.5	92.3	0.0	0.0	0.0
34: Deciduous	6203	0.4	12.1	3.0	0.3	0.0	0.0	0.0	1.3	2.5	0.1	0.0	0.0	80.4	0.0	0.0
35: Cloud	2449	0.0	0.0	0.0	0.0	0.0	6.2	0.0	0.0	0.0	0.0	0.0	0.0	0.0	93.8	0.0
36: Cloud Shadow	3253	3.5	0.3	0.0	0.0	0.0	0.0	0.0	0.1	0.0	0.0	2.4	0.0	0.0	0.0	93.7

Average accuracy = 72.0 Overall accuracy = 83.2 Kappa Coefficient = 0.82381

d) Confusion matrix of the pixel-based Euclidean classification for 2001 Landsat-7 ETM+

Areas		Percent Pixels Classified by Code													
Class	Pixels	1	5	6	11	13	16	18	19	26	30	31	34	39	40
1: Conifers	146387	82.1	14.5	0.0	0.0	0.0	0.0	2.7	0.0	0.0	0.4	0.0	0.3	0.0	0.2
5: Mixed Wood	2257	20.7	60.8	0.0	0.0	0.0	0.1	2.3	0.4	0.0	0.1	0.0	15.5	0.0	0.0
6: Regeneration	19489	0.6	5.1	69.3	0.0	0.0	0.1	2.5	7.7	0.2	0.2	0.0	14.3	0.0	0.0
11: Clear-cut 2001	8408	0.0	0.0	0.2	92.4	0.1	5.7	0.0	0.0	0.5	0.0	0.0	0.0	0.0	0.0
13: Rock	760	0.0	0.0	0.0	0.1	82.4	9.7	0.1	0.0	7.8	0.0	0.0	0.0	0.0	0.0
16: Clear Land	163	0.0	0.0	6.1	3.7	12.9	71.2	0.0	0.0	6.1	0.0	0.0	0.0	0.0	0.0
18: Scrub Coniferous	2949	2.9	12.5	16.1	0.0	0.0	0.0	43.5	24.8	0.0	0.0	0.0	0.2	0.0	0.0
19: Scrub Deciduous	1105	1.0	5.3	21.6	0.0	0.0	0.0	30.2	36.9	0.0	0.0	0.0	4.9	0.0	0.0
26: Mine	1001	11.0	0.0	1.8	0.6	14.1	14.0	10.5	0.7	45.8	0.6	1.0	0.0	0.0	0.0
30: Water Lake	2453	7.9	0.4	0.0	0.0	0.0	0.0	0.6	0.0	0.0	83.9	0.0	0.0	0.0	7.1
31: Water River	609	2.1	0.0	0.0	0.0	0.0	0.0	3.0	0.0	1.2	2.0	92.0	0.0	0.0	0.0
34: Deciduous	6203	0.2	10.6	4.2	0.0	0.0	0.6	0.9	1.8	0.0	0.0	0.0	81.7	0.0	0.0
39: Cloud	2712	0.0	0.0	0.0	0.0	6.8	0.5	0.0	0.0	0.2	0.0	0.0	0.0	92.6	0.0
40: Cloud Shadow	2502	0.1	0.0	0.0	0.0	0.0	0.0	0.0	0.0	0.0	2.6	0.0	0.0	0.0	97.2

Average accuracy = 73.7 Overall accuracy = 80.3 Kappa Coefficient = 0.79795

Appendix D. Confusion Matrix of spatial-based MLC/Adaptive Classification

a) Confusion matrix of the spatial-based MLC classification for 1985 Landsat-5 TM

Areas		Percent Pixels Classified by Code													
Class	Pixels	1	5	6	7	13	16	18	19	26	30	31	32	33	34
1: Conifers	180581	99.0	1.0	0.0	0.0	0.0	0.0	0.0	0.0	0.0	0.0	0.0	0.0	0.0	0.0
5: Mixed Wood	3309	5.8	65.5	0.0	0.0	0.0	0.0	8.4	0.0	0.0	0.0	0.0	0.0	0.0	20.3
6: Regeneration	3748	0.0	0.3	81.4	0.0	0.0	0.0	7.9	8.0	0.0	0.0	0.0	0.0	0.0	2.4
7: Clear-cut 1985	8140	0.0	0.0	0.4	99.0	0.0	0.6	0.0	0.0	0.0	0.0	0.0	0.0	0.0	0.0
13: Rock	760	0.0	0.0	0.0	0.0	89.5	0.0	0.0	0.0	10.5	0.0	0.0	0.0	0.0	0.0
16: Clear Land	163	0.0	0.0	0.0	0.0	0.0	100	0.0	0.0	0.0	0.0	0.0	0.0	0.0	0.0
18: Scrub Coniferous	3040	0.0	0.8	0.0	0.0	0.0	0.0	64.8	34.5	0.0	0.0	0.0	0.0	0.0	0.0
19: Scrub Deciduous	1392	0.0	0.0	0.0	0.0	0.0	0.0	16.2	83.8	0.0	0.0	0.0	0.0	0.0	0.0
26: Mine	1150	0.0	0.0	0.0	6.2	5.2	0.2	0.0	0.0	88.4	0.0	0.0	0.0	0.0	0.0
30: Water Lake	2453	0.0	0.0	0.0	0.0	0.0	0.0	0.0	0.0	0.0	89.7	0.0	0.0	10.3	0.0
31: Water River	609	0.0	0.0	0.0	0.0	0.0	0.0	0.0	0.0	0.0	0.0	100	0.0	0.0	0.0
32: Cloud	1449	0.0	0.0	0.0	0.0	0.0	0.0	0.0	0.0	0.0	0.0	0.0	100	0.0	0.0
33: Cloud Shadow	3031	0.0	0.0	0.0	0.0	0.0	0.0	0.0	0.0	0.0	0.0	0.0	0.0	100	0.0
34: Deciduous	6203	0.0	1.2	0.4	0.0	0.0	0.0	0.9	2.5	0.0	0.0	0.0	0.0	0.0	95.1

Average accuracy = 89.7% Overall accuracy = 97.3% Kappa Coefficient = 0.91225

b) Confusion matrix of the spatial-based MLC classification for 1990 Landsat-5 TM

Areas		Percent Pixels Classified by Code														
Class	Pixels	1	5	6	7	8	13	16	18	19	26	30	31	34	37	38
1: Conifers	179309	99.6	0.3	0.0	0.0	0.0	0.0	0.0	0.0	0.0	0.0	0.0	0.0	0.0	0.0	0.0
5: Mixed Wood	3193	10.4	74.1	0.0	0.0	0.0	0.0	0.0	0.0	1.4	0.0	0.0	0.0	14.1	0.0	0.0
6: Regeneration	3276	0.0	0.0	76.9	0.0	0.0	0.0	0.0	1.8	7.3	0.0	0.0	0.0	14.0	0.0	0.0
7: Regeneration	8070	0.0	0.0	3.3	91.7	3.6	0.0	0.1	0.9	0.4	0.0	0.0	0.0	0.0	0.0	0.0
8: Clear-cut 1990	6382	0.0	0.0	0.0	0.4	98.5	0.0	0.0	1.1	0.0	0.0	0.0	0.0	0.0	0.0	0.0
13: Rock	760	0.0	0.0	0.0	0.0	0.0	96.7	0.0	0.0	0.0	3.3	0.0	0.0	0.0	0.0	0.0
16: Clear Land	163	0.0	0.0	0.0	0.0	0.0	0.0	100	0.0	0.0	0.0	0.0	0.0	0.0	0.0	0.0
18: Scrub Coniferous	2243	0.2	9.0	0.0	0.0	0.0	0.0	0.0	65.7	23.9	0.0	0.0	0.0	1.2	0.0	0.0
19: Scrub Deciduous	1335	0.0	0.0	8.2	0.0	0.0	0.0	0.0	4.2	87.6	0.0	0.0	0.0	0.0	0.0	0.0
26: Mine	1121	0.0	0.0	0.0	0.0	0.0	2.5	13.3	0.0	0.0	84.2	0.0	0.0	0.0	0.0	0.0
30: Water Lake	2453	0.0	0.0	0.0	0.0	0.0	0.0	0.0	0.0	0.0	0.0	100	0.0	0.0	0.0	17.2
31: Water River	609	0.0	0.0	0.0	0.0	0.0	0.0	0.0	0.0	0.0	0.0	0.0	100	0.0	0.0	0.0
34: Deciduous	6203	0.0	2.7	0.8	0.0	0.0	0.0	0.0	0.0	3.7	0.0	0.0	0.0	92.8	0.0	0.0
37: Cloud	4912	0.0	0.0	0.0	0.0	0.0	0.0	0.0	0.0	0.0	0.0	0.0	0.0	0.0	100	0.0
38: Cloud Shadow	7110	0.0	0.0	0.0	0.0	0.0	0.2	0.0	0.0	0.0	0.0	0.0	0.0	0.0	0.0	99.8

Average accuracy = 91.2% Overall accuracy = 97.9% Kappa Coefficient = 0.94473

c) Confusion matrix of the spatial-based Adaptive classification for 1996 Landsat-5 TM

Areas		Percent Pixels Classified by Code													
Class	Pixels	1	5	6	10	13	16	18	19	26	30	31	34	35	36
1: Conifers	179804	99.5	0.2	0.0	0.0	0.1	0.0	0.1	0.0	0.0	0.0	0.0	0.0	0.0	0.2
5: Mixed Wood	2230	14.0	70.2	0.0	0.0	0.0	0.0	0.0	0.0	0.0	0.0	0.0	15.8	0.0	0.0
6: Regeneration	8305	0.6	1.0	58.4	0.2	0.0	20.7	0.8	0.0	0.0	0.0	0.0	5.3	13.0	0.0
10: Clear-cut 1996	6647	0.0	0.0	0.0	99.5	0.0	0.5	0.0	0.0	0.0	0.0	0.0	0.0	0.0	0.0
13: Rock	760	0.0	0.0	0.0	0.0	89.5	0.0	0.0	0.0	10.5	0.0	0.0	0.0	0.0	0.0
16: Clear Land	163	0.0	0.0	0.0	0.0	30.1	69.3	0.0	0.0	0.0	0.0	0.0	0.0	0.0	0.0
18: Scrub Coniferous	2949	0.0	0.6	0.0	0.0	0.0	0.0	97.6	0.7	0.0	0.0	0.0	1.1	0.0	0.0
19: Scrub Deciduous	1105	0.0	0.0	5.5	0.0	0.0	0.0	71.0	23.5	0.0	0.0	0.0	0.0	0.0	0.0
26: Mine	2346	8.7	0.0	0.0	0.0	2.2	14.2	0.0	0.0	66.7	0.0	0.0	0.0	7.8	0.0
30: Water Lake	2453	0.0	0.0	0.0	0.0	0.0	0.0	0.0	0.0	0.0	100	0.0	0.0	0.0	0.0
31: Water River	609	0.0	0.0	0.0	0.0	0.0	0.0	0.0	0.0	0.0	0.0	100	0.0	0.0	0.0
34: Deciduous	6203	0.0	1.7	2.4	0.0	0.0	0.0	0.8	0.0	0.0	0.0	0.0	96.0	0.0	0.0
35: Cloud	2449	0.0	0.0	0.0	0.0	0.0	0.0	0.0	0.0	0.0	0.0	0.0	0.0	100	0.0
36: Cloud Shadow	3253	0.0	0.0	0.0	0.0	2.0	0.0	0.0	0.0	0.0	0.0	0.0	0.0	0.0	98.0

Average accuracy = 83.4% Overall accuracy = 96.7% Kappa Coefficient = 0.89893

d) Confusion matrix of the spatial-based MLC classification for 2001 Landsat-7 ETM+

Areas		Percent Pixels Classified by Code													
Class	Pixels	1	5	6	11	13	16	18	19	26	30	31	34	39	40
1: Conifers	146387	96.6	1.0	0.3	0.0	0.0	0.1	1.7	0.3	0.0	0.1	0.0	0.0	0.0	0.1
5: Mixed Wood	2257	11.7	71.9	0.0	0.0	0.0	0.0	0.5	0.0	0.0	0.0	0.0	16.0	0.0	0.0
6: Regeneration	19489	0.1	7.6	67.4	0.0	0.0	0.6	4.1	10.6	0.0	0.3	0.5	9.0	0.0	0.0
11: Clear-cut 2001	8408	0.0	0.0	0.7	95.5	0.0	3.4	0.1	0.2	0.0	0.0	0.0	0.0	0.0	0.0
13: Rock	760	0.0	0.0	0.0	0.0	92.9	3.8	0.0	0.0	3.3	0.0	0.0	0.0	0.0	0.0
16: Clear Land	163	0.0	0.0	0.0	0.0	0.0	100	0.0	0.0	0.0	0.0	0.0	0.0	0.0	0.0
18: Scrub Coniferous	2949	0.8	1.7	0.7	0.0	0.0	0.0	94.2	2.4	0.0	0.0	0.0	0.0	0.0	0.0
19: Scrub Deciduous	1105	0.3	0.0	0.0	0.0	0.0	0.0	29.9	69.9	0.0	0.0	0.0	0.0	0.0	0.0
26: Mine	1001	0.0	0.0	0.0	0.0	0.0	2.0	0.0	0.0	97.5	0.5	0.0	0.0	0.0	0.0
30: Water Lake	2453	0.0	0.0	0.0	0.0	0.0	0.0	0.0	0.0	0.0	100	0.0	0.0	0.0	0.0
31: Water River	609	0.0	0.0	0.0	0.0	0.0	0.0	0.0	0.0	0.0	0.0	100	0.0	0.0	0.0
34: Deciduous	6203	0.0	4.2	1.9	0.0	0.0	0.3	0.0	0.8	0.0	0.0	0.0	92.7	0.0	0.0
39: Cloud	2712	0.0	0.0	0.0	0.0	0.0	0.0	0.0	0.0	0.0	0.0	0.0	0.0	100	0.0
40: Cloud Shadow	2502	0.5	0.0	0.0	0.0	0.0	0.0	0.0	0.0	0.4	13.4	0.0	0.0	0.0	85.7

Average accuracy = 90.3% Overall accuracy = 93.0% Kappa Coefficient = 0.84603